

# Query-Based Asymmetric Modeling with Decoupled Input-Output Rates for Speech Restoration

Ui-Hyeop Shin<sup>1</sup> Jaehyun Ko<sup>2</sup> Woocheol Jeong<sup>2</sup> Hyung-Min Park<sup>1,2</sup>

## Abstract

Speech restoration in real-world conditions is challenging due to compounded distortions and mismatches between input and desired output rates. Most existing systems assume a fixed and shared input–output rate, relying on external resampling that confines learning to a specific target resolution and limits model generality. We address this setting by formulating speech restoration under decoupled input–output rates, and propose TF-Restormer, a query-based asymmetric modeling framework. The encoder concentrates analysis on the observed input bandwidth using a time–frequency dual-path architecture, while a lightweight decoder reconstructs missing spectral content via frequency extension queries. This design enables a single model to operate consistently across arbitrary input–output rate pairs without redundant resampling. Experiments across diverse sampling rates, degradations, and operating modes show that TF-Restormer maintains stable restoration behavior and balanced perceptual quality, including in real-time streaming scenarios. Anonymous code and demos are available at <https://tf-restormer.github.io/demo>.

## 1. Introduction

Speech enhancement (Ephraim & Malah, 1984; Pascual et al., 2017) has historically progressed through isolated sub-tasks with dedicated models such as denoising (Hu et al., 2020; Ho et al., 2020), dereverberation (Han et al., 2015; Wang & Wang, 2020), declipping (Mack & Habets, 2019), and bandwidth extension or super-resolution (Liu et al., 2022a; Lee & Han, 2021). In real-world settings, multiple distortions often coincide and further obscure both magnitude and phase, making coherent and faithful speech

<sup>1</sup>Department of Electronic Engineering, University of Sogang, Seoul, Korea <sup>2</sup>Department of Artificial Intelligence, University of Sogang, Seoul, Korea. Correspondence to: Hyung-Min Park <hpark@sogang.ac.kr>.

restoration substantially more difficult. Crucially, this complexity is often accompanied by a fundamental mismatch between the native input bandwidth and the desired output sampling rate, a challenge that remains largely unaddressed by conventional task-specific frameworks.

This growing complexity has prompted a shift towards *general speech restoration* using generative models to handle diverse distortions (Liu et al., 2022b; Serrà et al., 2022). Vocoder (Kumar et al., 2019; Kong et al., 2020a)-based approaches reconstruct waveforms from compressed representations (Liu et al., 2022b; Babaev et al., 2024). While such approaches improve perceptual quality, they discard phase information and treat speech as a semantic abstraction rather than a physical signal. In contrast, waveform or complex-spectrum-based generative models (Ord et al., 2016; Serrà et al., 2022; Welker et al., 2022; Richter et al., 2023) including GAN- and diffusion-based methods operate directly on the waveform or complex STFT with improved fidelity, but their temporal compression or iterative sampling precludes streaming.

Beyond the choice of generative modeling paradigm, a critical and often overlooked limitation of existing approaches lies in their assumption of *a fixed and shared input–output sampling rate*. Restoration models, as well as dedicated super-resolution methods (Kim et al., 2024; Lu et al., 2025), typically begin by resampling the input signal to a predetermined target rate before processing. While this design choice simplifies training by fixing the spectral resolution, it also tightly couples the learned representations to a specific output grid. As a result, every input must be converted to the target rate regardless of its native bandwidth, leading to redundant resampling and resolution-specific modeling. Moreover, supporting multiple output rates under this paradigm requires either training separate models or repeatedly upsampling and downsampling, further entangling the learning process with a fixed resolution assumption. These limitations call for a universal framework that analyzes the observed input bandwidth directly and synthesizes arbitrary output rates without relying on external resampling.

In parallel, denoising and separation models have been extensively developed in the complex STFT domain (Choi et al., 2018; Hu et al., 2020). More recently, time–frequency (TF) dual-path models have been introduced (Dang et al.,

2022; Wang et al., 2023), which alternate sequence modeling along the time and frequency axes. By treating frequency bins as sequences rather than static feature dimensions, these models preserve spectral structures and achieve strong performance. This formulation naturally supports sampling-frequency-independent (SFI) processing (Paulus & Torcoli, 2022; Zhang et al., 2023), as the frequency axis can be viewed as a sequence scaling with the input sampling rate while maintaining a consistent STFT frame duration. However, existing TF models still assume matched input–output rates. Moreover, because they preserve fine-grained spectral representations throughout the network, their computational cost grows substantially at higher sampling rates, limiting direct application to super-resolution.

These observations motivate a new design that retains the strengths of TF dual-path processing while addressing a setting in which the standard learning assumption of matched input–output resolutions no longer holds. To this end, we propose *TF-Restormer*, an asymmetric encoder–decoder architecture for speech restoration under diverse degradations. Inspired by masked autoencoders (MAE) (He et al., 2022), TF-Restormer concentrates heavy computation in a TF dual-path encoder that analyzes the observed input bandwidth, while a lightweight decoder reconstructs missing high-frequency components through learnable *extension queries* using a cross-self attention mechanism (Gupta et al., 2023). By explicitly separating input-band analysis from output-band synthesis, this asymmetric design enables a single model to operate across arbitrary input–output sampling rate pairs without external resampling, while preserving physical signal fidelity.

In summary, our contributions are as follows:

- We formulate speech restoration under *decoupled input–output sampling rates*, where the standard learning assumption of matched spectral resolutions no longer holds, and propose a *query-based asymmetric* TF encoder–decoder that analyzes the input bandwidth and synthesizes arbitrary output rates without external resampling.
- Our asymmetric design enables a *single model* to support general speech restoration including super-resolution, across heterogeneous input–output rate pairs, with unified training facilitated by a shared sampling-frequency-independent (SFI) STFT discriminator.
- We improve robustness and practicality by enhancing the frequency module with a projection-based *spectral inductive bias* and extending the time module to a causal variant, enabling stable restoration under severe degradations and real-time streaming inference.
- We propose a *scaled log-spectral loss* as an auxiliary objective that stabilizes training under extreme distortions while mitigating oversmoothing, complementing perceptual (Babaev et al., 2024) and adversarial training (Mao et al., 2017).

## 2. Related Work

**Vocoder- and diffusion-based restoration** Generative approaches have significantly improved speech quality. Vocoder systems typically project speech into Mel features (Liu et al., 2022b; Babaev et al., 2024) or learned representations (Koizumi et al., 2023; Li et al., 2024) and synthesize waveforms with neural vocoders (Oord et al., 2016; Kumar et al., 2019; Kong et al., 2020a). They often achieve “studio-like” perceptual quality but reduce signal fidelity, since intermediate features serve as perceptual cues rather than physical signals. Diffusion-based methods from waveform (Kong et al., 2020b; Serrà et al., 2022; Welker et al., 2022; Scheibler et al., 2024) or STFT inputs (Lemercier et al., 2023; Richter et al., 2023) excel at generating diverse realizations. However, each approach often relies on temporal compression or iterative sampling, limiting real-time streaming. More critically, both paradigms are typically bound to a fixed-rate assumption, requiring external resampling to match a specific target bandwidth. In contrast, we propose a single-pass complex spectral prediction framework that avoids the abstraction bottleneck of vocoders and the complexity of diffusion, while supporting variable input–output rates through an asymmetric design.

**TF dual-path models** TF dual-path models (Dang et al., 2022) alternate sequence modeling along time and frequency, preserving spectral structure and naturally supporting sampling-frequency-independent (SFI) designs (Zhang et al., 2023). They have shown strong performance in enhancement (Cao et al., 2022; Lu et al., 2023; Chao et al., 2024) and separation (Wang et al., 2023; Saijo et al., 2024; Shin et al., 2025). However, most prior models employ symmetric block designs for time and frequency processing, despite the distinct statistical characteristics of the two domains. Under challenging degradations, this limitation becomes more pronounced, motivating the use of projection-based frequency modules that inject spectral inductive bias for more robust high-frequency recovery. Furthermore, while existing dual-path models assume matched input–output rates, we extend this paradigm with an asymmetric encoder–decoder structure that explicitly supports restoration under decoupled rates.

**Audio super-resolution** Conventional super-resolution models (Liu et al., 2022a; Han & Lee, 2022; Kim et al., 2024; Lu et al., 2025) typically assume a fixed target rate, upsampling inputs before processing to fill missing bands. While effective, this introduces redundancy and ties each model to a single output rate. Our framework moves beyond this fixed-rate constraint by framing super-resolution as a conditional spectral completion. Using *frequency extension queries* within an asymmetric encoder–decoder, TF-Restormer confines heavy processing to the input bandwidth and restores missing bands as needed, supporting arbitrary, user-specified output rates without rate-specific models.

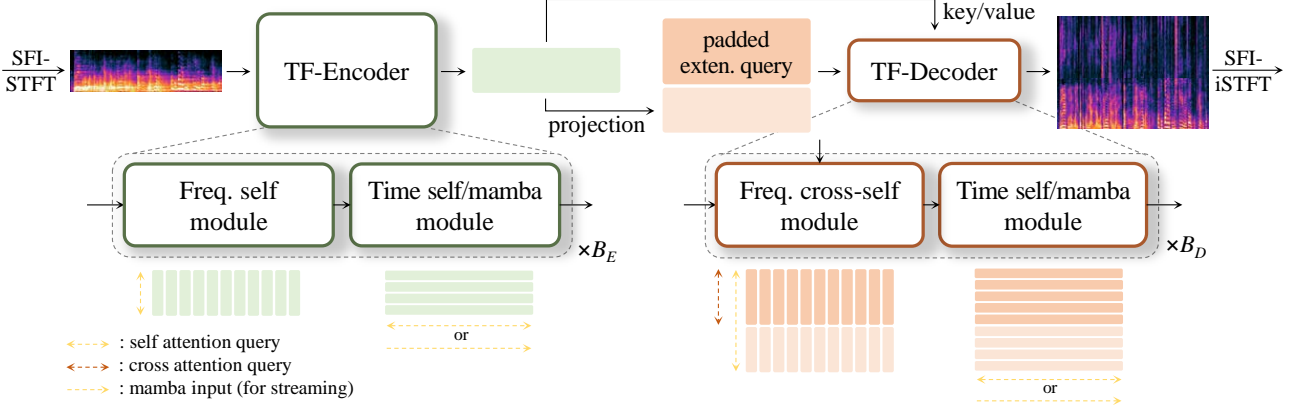


**Figure 1. Overall architecture of TF-Restormer.** The framework employs a query-based asymmetric design to handle decoupled input–output rates. The heavy TF-Encoder focuses on analysis within the native input bandwidth, while the lightweight TF-Decoder reconstructs missing high-frequency bands using learnable extension queries, bypassing the need for redundant resampling.

### 3. TF-Restormer

#### 3.1. SFI input–output formulation

As an SFI model (Paulus & Torcoli, 2022), TF-Restormer addresses arbitrary input sampling rates  $f_E$  by constructing STFT with a constant frame duration (SFI-STFT). Unlike conventional SFI that assumes matched input–output rates, we introduce the first *decoupled formulation*, enabling inference at user-specified output rates  $f_D$ . Given an input  $x \in \mathbb{R}^{1 \times N_E}$  with sampling rate  $f_E$ , its STFT is  $\mathbf{X} \in \mathbb{R}^{F_E \times T \times 2}$ , where  $F_E$  and  $T$  are the number of frequency bins and frames. TF-Restormer then predicts  $\mathbf{Y} \in \mathbb{R}^{F_D \times T \times 2}$  corresponding to an output  $y \in \mathbb{R}^{1 \times N_D}$  at sampling rate  $f_D$ , satisfying  $f_E : f_D = (F_E - 1) : (F_D - 1)$  under the assumption of consistent frame duration. To ensure universal applicability across sampling rates, we adopt a 40 ms analysis window with a 20 ms hop. This choice is a common unit in speech analysis and, being integer multiples across typical rates, guarantees consistent STFT construction at  $\{8, 16, 22.05, 24, 32, 44.1, 48\}$  kHz without requiring resampling. The maximum number of frequency bins  $F_{\max}$  is 961 for  $f_E = 48$ kHz.

#### 3.2. Analysis encoder and extension decoder

**TF-encoder for input analysis** As illustrated in Figure 1, the TF-Restormer is constructed with TF-encoder and TF-decoder. The TF-encoder is responsible for analyzing the speech component from the input signals  $\mathbf{X}$ . Before the TF-encoder, the input complex representation  $\mathbf{X}$  is first projected to  $C_E$  dimension by 2d convolution (Conv2D) layer with kernel size of (3,3), followed by layer normalization (LN) (Ba et al., 2016). Then, positional embeddings are added along the frequency axis. In the encoder, the projected feature is alternately processed by freq. and time self modules  $B_E$  times to capture speech component.

**TF-decoder with extension query** The encoder features  $\mathbf{Z} \in \mathbb{R}^{F_E \times T \times C_E}$  are projected into the decoder space with  $C_D$  to serve as both the initial features and the key/value pairs for the frequency cross-self module. To reconstruct the missing high-frequency regions beyond the observed bandwidth, we introduce learnable extension queries,  $\mathbf{Q}_{\text{ext}} = [\mathbf{q}_{F_E+1}, \dots, \mathbf{q}_{F_D}]^T \in \mathbb{R}^{(F_D - F_E) \times C_D}$ , where  $\mathbf{q}_f \in \mathbb{R}^{C_D}$  is a frequency-wise learnable vector. Instead of simple zero-padding, these queries function as frequency-specific latent priors optimized to capture the characteristics of each sub-band. By slicing these queries from a unified master vector  $\tilde{\mathbf{Q}}_{\text{ext}}$  defined over  $[F_{\min}, F_{\max}]$ , the decoder maintains consistent spectral alignment regardless of the specific input or output sampling rates. This ensures that the model treats a specific frequency bin with the same learned representation, facilitating rate-invariant generalization. In the frequency cross-self module, these queries explicitly guide the cross-attention mechanism to retrieve relevant acoustic context from the encoder features. Finally, the complex STFT values  $\mathbf{Y}$  are estimated from the decoder features through a Conv2D layer.

#### 3.3. Asymmetric TF dual-path module

In TF dual-path modules, given the feature with shape  $\mathbb{R}^{T \times F \times C}$  where  $F \in \{F_E, F_D\}$ , time modules process  $F$  sequences with lengths of  $T$  while frequency modules consider the feature as  $T$  sequences with lengths of  $F$  as illustrated in Figure 1. As shown in Figure 2(a), time self module consists of two macaron-style (Lu\* et al., 2019) convolution feed-forward network (ConvFFN) with Conv1D with kernel size  $K$  for capturing local contexts (Saijo et al., 2024). In ConvFFN, the expansion factor is 3 with SwiGLU as hidden activation. Between ConvFFN modules, multi-head self-attention (MHSA) is used for global contexts with  $H$  heads. The time module performs MHSA on temporal frames with rotary positional encoding (RoPE) (Su et al.,

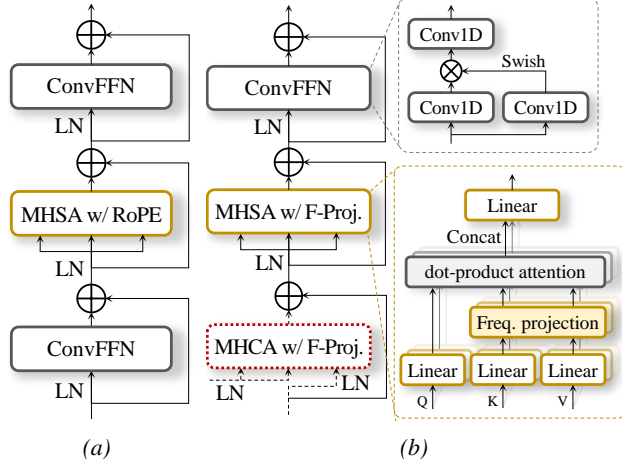


Figure 2. Unit modules in TF-encoder and decoder is based on (a) the time self module based on MHSA with RoPE and (b) the frequency module based on MHSA with frequency projection layer. The frequency cross-self module employs MHCA based on key/value from the encoder features while frequency self module is based on two ConvFFNs similarity to time self module.

2024) to offer the relative positions. On the other hand, the frequency self module applies MHSA with the frequency projection layer to induce the structural bias as frequency bins are more static sequence with a fixed length, exhibiting a relatively consistent structural roles.

**Frequency cross-self module** As illustrated in Figure 1 and 2(b), the freq. cross-self module in the decoder distinguishes between observed and unobserved frequency bins at the level of query construction. Specifically, for MHSA, the entire frequency axis is treated symmetrically, and all frequency bins participate as queries, keys, and values. In contrast, MHCA is applied only to the unobserved high-frequency region  $\mathbf{Q}_{\text{ext}}$  when  $f_E < f_D$ , while the key-value are derived from the encoder features  $\mathbf{Z}$  corresponding to the observed input bandwidth. Therefore, when  $f_E = f_D$ , no extension queries are instantiated and the MHCA path is bypassed entirely.

**Attention with structural bias** Linformer (Wang et al., 2020) introduced linear projections of key-value to reduce the computations, while MLP-Mixer (Tolstikhin et al., 2021) entirely replaced MHSA with static linear operations. Motivated by these insights (Quan & Li, 2024), we incorporate a frequency linear projection (Figure 2(b)) to impose an inductive bias for the structural consistency of frequency bins on top of the benefits of dynamic attention. Since frequency bins exhibit consistent characteristics and considering the former studies (Wang et al., 2020; Quan & Li, 2024), we share the same projection layer across all modules and key-value mappings. Formally, for each head  $h=1, \dots, H$ , given key-value  $\mathbf{K}_{h,c}, \mathbf{V}_{h,c} \in \mathbb{R}^{T \times F}$  at channel  $c$ , a projection matrix  $\mathbf{A}_h \in \mathbb{R}^{F_{\text{max}} \times F_{\text{proj}}}$  with dimension  $F_{\text{proj}}$  and maximum bins  $F_{\text{max}}$  is applied as

$$\tilde{\mathbf{K}}_{h,c} = [\mathbf{K}_{h,c}, \mathbf{O}] \mathbf{A}_h \in \mathbb{R}^{T \times F_{\text{proj}}}, \quad 1 \leq c \leq C_h, \quad (1)$$

$$\tilde{\mathbf{V}}_{h,c} = [\mathbf{V}_{h,c}, \mathbf{O}] \mathbf{A}_h \in \mathbb{R}^{T \times F_{\text{proj}}}, \quad 1 \leq c \leq C_h, \quad (2)$$

where  $\mathbf{O} \in \mathbb{R}^{T \times (F_{\text{max}} - F)}$  is a zero-padding matrix.

**Streaming mode with mamba** The modular design of TF dual-path model further enables a seamless extension to streaming mode by replacing the time module with Mamba (Gu & Dao, 2024) blocks. Refer to Appendix B for detailed model configurations.

## 4. Training

The model is trained by two phases of pretraining and adversarial training. The model is trained with  $f_D$  randomly selected from  $\{16, 24, 44.1, 48\}$  kHz at each step by down-sampling target speech signals from VCTK dataset (Yamagishi et al., 2019). Based on speech sources, we simulated noisy reverberant signals by convolving the room impulse response (RIR) and noise samples from the DNS dataset (Reddy et al., 2020). We then applied various digital distortions including codecs and downsampled the signal to the sampling rates  $f_E$  of 8k or 16kHz, which are common in practical restoration condition (see Appendix A.1 for details). Because extension query could be undertrained if distribution of the input and output sample rates is unbalanced in training, we investigate these issue in Appendix E.

### 4.1. Pretraining

**Perceptual loss** Following (Babaev et al., 2024), we incorporate a self-supervised learning (SSL)-based perceptual loss to stabilize adversarial training and encourage human-aligned quality. Specifically, extracting features from a pretrained SSL model for both the enhanced and clean waveforms, we minimize the mean-squared-error between these representations:

$$\mathcal{L}_p(\theta) = \mathbb{E}_{m,n} [ |\phi(g_\theta(x))_{m,n} - \phi(s)_{m,n}|^2 ], \quad (3)$$

given that  $y = g_\theta(x)$  is output of restoration model  $g_\theta(\cdot)$  with parameters of  $\theta$ .  $\phi(\cdot)_{m,n}$  denotes the  $m$ -th element of  $n$ -th frame from its feature map. We utilize WavLM-conv (Chen et al., 2022b) as in the previous study (Babaev et al., 2024).

**Proposed scaled log-spectral loss** Because the perceptual loss is restricted to 16 kHz and it is beneficial to guide spectral details to complement the looseness of perceptual loss, a previous work adopted an  $\ell_1$  distance on the magnitude spectrum (Babaev et al., 2024). However, because TF-Restormer operates directly on the complex spectrum, the model can be explicitly supervised on both real and imaginary components in addition to the magnitude. Therefore, when denoting the STFT of target signal  $s$  by  $S_{r,tf} = |S_{r,tf} + jS_{i,tf}|$  and that of model's predicted signal  $g_\theta(x)$  by  $Y_{r,tf} = |Y_{r,tf} + jY_{i,tf}|$ , we can extend to the

complex domain as  $\mathcal{L}_{\ell_1}(\theta) = \sum_{c \in \mathcal{C}} \alpha_c \cdot \mathbb{E}_{t,f} [|Y_{c,tf} - S_{c,tf}|]$ , where  $\mathcal{C} = \{r, i, m\}$  denotes the component index set and  $\alpha_c$  are component weights.

However, even with complex supervision, while some regions are relatively easy to predict and receive consistent gradients, severely degraded or missing high-frequency regions yield unstable gradients and drive the model toward oversmoothing, or averaging, effects (Babaev et al., 2024). To address this, we propose a *scaled log-spectral loss* selectively emphasizing well-predicted regions while preventing poorly predicted regions from dominating:

$$\mathcal{L}_s(\theta) = \sum_{c \in \mathcal{C}} \alpha_c \cdot \mathbb{E}_{t,f} \left[ w_{tf} \log \left( 1 + \frac{|Y_{c,tf} - S_{c,tf}|}{w_{tf}} \right) \right], \quad (4)$$

where  $w_{tf}$  is scale factor that controls the relative scaling of gradient. The formulation  $w \log(1 + d/w)$  ensures large gradients on smaller distance  $d$  than  $w$ , preserving regions where phase and magnitude are already reconstructed well, while suppressing the influence of large deviations, avoiding the averaging common in  $\ell_1$  or  $\ell_2$  losses. For choosing the weight value  $w_{tf}$ , we empirically observed that a distance  $|Y_{c,tf} - S_{c,tf}|$  tends to be proportional to the source  $|S_{m,tf}|$ . Therefore,  $w_{tf}$  is set to  $E[S_{m,tf}]$  by averaging over the frames. We use  $\alpha_m = 0.6$ ,  $\alpha_r = 0.2$ , and  $\alpha_i = 0.2$ . Finally, when combined with the perceptual loss, our proposed objective becomes  $\mathcal{L}_{\text{pre}}(\theta) = \lambda_p \mathcal{L}_p(\theta) + \lambda_s \mathcal{L}_s(\theta)$  where  $\lambda_*$  denote loss weighting factors. Therefore, perceptual loss mainly focuses on largely deviated component while the scaled log-spectral more on well-predicted component, making them complementary to each other. For pretraining, we train the TF-Restormer with  $\lambda_p = 100$  and  $\lambda_s = 1$ .

## 4.2. Adversarial training

After pretraining the generator with  $\mathcal{L}_{\text{pre}}$ , we introduce an adversarial loss component to reduce the artifacts and predict severely distorted or missing components. For adversarial training, we attach multi-scale STFT discriminators (Défossez et al., 2023) as  $i$ -th discriminator of  $\varphi_i$  and apply least square GAN (LS-GAN) loss (Mao et al., 2017). For generator, generator LS-GAN and feature-matching loss (Kumar et al., 2019) terms are added, respectively:

$$\begin{aligned} \mathcal{L}_{\text{gen}}(\theta) &= \lambda_g \mathcal{L}_g(\theta) + \lambda_{\text{fm}} \mathcal{L}_{\text{fm}}(\theta) \\ &\quad + \lambda_p \mathcal{L}_p(\theta) + \lambda_s \mathcal{L}_s(\theta) + \lambda_{\text{hf}} \mathcal{L}_{\text{hf}}(\theta), \end{aligned} \quad (5)$$

$$\mathcal{L}_{\text{disc}}(\varphi_i) = \mathcal{L}_d(\varphi_i), \quad i = 1, \dots, I. \quad (6)$$

where  $\mathcal{L}_{\text{hf}} = \mathcal{L}_{\text{pesq}} + 10 \cdot \mathcal{L}_{\text{utmos}}$  is additional human-feedback loss (Babaev et al., 2024) for aesthetic quality with differentiable PESQ loss and UTMOS loss (Saeki et al., 2022). We performed adversarial training using  $\mathcal{L}_{\text{gen}}(\theta)$  with  $\lambda_g = 0.005$ ,  $\lambda_{\text{fm}} = 0.1$ ,  $\lambda_p = 100$ ,  $\lambda_s = 1$ , and  $\lambda_{\text{hf}} = 0.0001$ . Notably, we assign small weights to  $\mathcal{L}_g$  and  $\mathcal{L}_{\text{hf}}$  to avoid excessive generation artifacts.

**Proposed multi-scale SFI-STFT discriminators** In conventional adversarial training, a dedicated generator for each target sampling rate is trained with a corresponding discriminator as well (Défossez et al., 2023; Babaev et al., 2024; Ju et al., 2024), which introduces implementation overhead depending on the output sample rates. For training of a single generator across diverse rates, we propose a discriminator based on SFI-STFT, which preserves a consistent physical frame duration across sampling rates. Implemented with strided Conv2D layers, STFT discriminator (Défossez et al., 2023) produces two-dimensional maps that provide local real/fake supervision in the time-frequency plane. This design maintains sensitivity to spectral structure while remaining agnostic to absolute frequency resolution, thereby supporting adversarial training across different rates without redundant resampling or multiple discriminators. We employ 5 SFI discriminators with STFT window durations of  $\{20, 40, 60, 80, 100\}$  ms.

## 5. Evaluation

### 5.1. Test dataset and metrics

We evaluate a unified TF-Restormer for various datasets to validate the robustness across heterogeneous distortion conditions and arbitrary input–output sample-rates. For denoising(DN) and speech super-resolution (SSR), we also reports dedicated version of TF-Restormer for fair comparison and training configuration for dedicated models are summarized in Appendix A.3.

#### UNIVERSE data for general speech restoration (GSR)

As GSR model, we evaluate on 100 synthetic samples generated by UNIVERSE authors (Serrà et al., 2022) to ensure comparability to prior works in  $f_E = f_D = 16\text{kHz}$  setting. The dataset introduces diverse simulated degradations such as bandpass filtering, reverberation, codec compression, and transmission artifacts.

**VCTK-DEMAND for DN** We additionally evaluated the well-known Valentini denoising dataset (Valentini-Botinhao & others, 2017) for direct comparison with conventional enhancement models as speech enhancement benchmarking. The evaluation set (824 utterances) consists of noisy mixtures from two speakers under four SNR conditions (17.5, 12.5, 7.5, and 2.5 dB).

**VCTK for SSR** For SSR evaluation, we construct paired data by downsampling 48 kHz clean utterances from the VCTK-0.92 dataset (Yamagishi et al., 2019). Beyond the clean case, we also create noisy-distorted conditions by adding degradations such as noise, reverberation, band-pass filtering, and codec effects, enabling a comprehensive evaluation of GSR with SSR. Note that the training simulation follows a similar procedure, which may provide a slight advantage to our model.

Table 1. Results on UNIVERSE data for GSR. <sup>†</sup>We utilized pretrained models from implementation code from UNIVERSE++ (Scheibler et al., 2024). <sup>‡</sup>The results are reported in the original paper (Babaev et al., 2024)

Model	Signal fidelity			Perceptual quality			
	PESQ <sup>†</sup>	SDR <sup>†</sup>	LSD <sup>†</sup>	MCD <sup>†</sup>	sBERT <sup>†</sup>	UTMOS <sup>†</sup>	DNSMOS <sup>†</sup>
Input	1.55	5.58	1.89	10.21	0.84	2.19	2.23
Ground Truth	4.50	$\infty$	0.00	0.00	1.00	4.26	3.33
VoiceFixer	1.77	-5.68	1.49	10.50	0.84	2.83	2.99
StoRM	1.76	9.01	1.67	6.87	0.84	2.70	2.94
UNIVERSE <sup>†</sup>	1.74	7.73	1.92	6.25	0.79	2.64	2.73
UNIVERSE++ <sup>‡</sup>	1.80	8.42	1.76	5.96	0.81	2.71	2.82
TF-Locoformer	2.13	<b>11.61</b>	2.00	6.26	0.89	2.95	2.86
FINALLY	-	-	-	-	-	<b>4.21<sup>‡</sup></b>	3.25 <sup>‡</sup>
TF-Restormer (off)	<b>2.30</b>	11.12	<b>1.45</b>	<b>5.08</b>	<b>0.91</b>	4.08	<b>3.25</b>
TF-Restormer (on)	2.00	8.89	1.47	6.01	0.87	3.77	3.14

For the evaluation, we adopt non-intrusive perceptual estimators for mean opinion score (MOS): DNSMOS (Reddy et al., 2022), UTMOS (Saeki et al., 2022), and NISQA (Mittag et al., 2021) to assess the perceptual quality. Also, to assess the perceptual signal fidelity of restored signal compared to the reference, we employ perceptual evaluation of speech quality (PESQ) (Rix et al., 2001), signal-to-distortion ratio (SDR) (Le Roux et al., 2019), log-spectral distance (LSD), mel-cepstral distortion (MCD) (Fukada et al., 1992). In addition, to evaluate the reference-aware speech generation quality by capturing semantic congruence, we report SpeechBERTScore(sBERT) (Saeki et al., 2024).

## 5.2. Validation of stability across diverse scenarios

In this section, we validate the operational stability of TF-Restormer across a wide spectrum of restoration scenarios. For the UNIVERSE dataset, we consider VoiceFixer (Liu et al., 2022b) as a Mel vocoder-based baseline, StoRM (Lemercier et al., 2023), UNIVERSE (Serrà et al., 2022), and UNIVERSE++ (Scheibler et al., 2024) as diffusion-based baselines, TF-Locoformer as a recent TF dual-path Transformer model, and FINALLY (Babaev et al., 2024) as a latest strong Mel-vocoder method. As shown in Table 1, VoiceFixer improves MOS but sacrifices fidelity due to its Mel representation, while FINALLY achieves the highest perceptual quality yet lacks signal fidelity, a trend confirmed in Table 2. Diffusion-based methods yield more balanced results by directly operating in the waveform or complex STFT. TF-Locoformer preserves signal-level fidelity but suffers from residual perceptual artifacts and failure to recover lost details and naturalness (MOS, LSD). In contrast, TF-Restormer provides balanced improvements for signal fidelity and perceptual quality, with its streaming variant maintaining competitive effectiveness under causal constraints. This indicates its robustness across diverse degradations in a universal restoration setting. Note that all the compared models are offline methods.

Next, we evaluate TF-Restormer on the VCTK+DEMAND

Table 2. Results on VCTK-DEMAND for denoising task. <sup>†</sup>Dedicated models trained specifically for denoising.

Model	Signal fidelity				Perceptual quality		
	PESQ <sup>†</sup>	SDR <sup>†</sup>	LSD <sup>†</sup>	MCD <sup>†</sup>	sBERT <sup>†</sup>	UTMOS <sup>†</sup>	DNSMOS <sup>†</sup>
Input	1.98	8.56	1.27	5.40	0.91	2.90	2.45
Ground Truth	4.50	$\infty$	0.00	0.00	1.00	4.07	3.16
DB-AIAT	3.27	21.30	0.90	1.77	0.95	3.83	3.13
MP-SENet	3.61	21.03	0.85	1.58	0.95	3.86	3.12
TF-Locoformer	3.30	<b>23.82</b>	0.92	3.58	0.95	3.93	3.20
VoiceFixer	2.40	-1.12	0.97	7.40	0.90	3.50	3.08
UNIVERSE	2.84	18.77	1.17	2.20	0.92	3.75	3.03
FINALLY	2.94	4.60	-	-	-	<b>4.32</b>	<b>3.22</b>
TF-Restormer (off)	3.41	19.45	0.75	1.54	<b>0.95</b>	4.14	3.14
TF-Restormer (off) <sup>‡</sup>	<b>3.63</b>	22.81	<b>0.73</b>	<b>1.49</b>	0.95	4.04	3.13
TF-Restormer (on)	2.89	16.43	0.85	2.16	0.93	4.05	3.09

Table 3. Results on VCTK for SSR under clean and noisy-distorted conditions. <sup>†</sup>The models require fixed output sampling rates  $f'$ , thus evaluated by upsampling the input of  $f_E$  to  $f' \geq f_D$  and downsampling the output back to the target rate  $f_D$ . <sup>‡</sup>Dedicated models trained specifically for super-resolution.

Method	8 → 16kHz				8 → 24kHz				8 → 44.1kHz				16 → 48kHz				
	LSD <sup>†</sup>	NISQA <sup>†</sup>	clean (SSR only)	LSD <sup>†</sup>	NISQA <sup>†</sup>	LSD <sup>†</sup>	NISQA <sup>†</sup>	clean (SSR only)	LSD <sup>†</sup>	NISQA <sup>†</sup>							
Input	2.53	3.78	2.91	3.78	3.44	3.78	3.17	4.40									
NVSR <sup>†</sup>	0.83	4.15	0.89	4.24	0.94	4.16	-	-									
Freepainter <sup>†</sup>	1.33	3.94	1.40	3.79	1.37	3.71	1.31	4.01									
AP-BWE <sup>†</sup>	0.90	4.20	0.86	4.34	0.88	4.26	0.85	4.33									
VoiceFixer <sup>†</sup>	1.05	4.20	1.05	4.27	1.06	4.21	-	-									
TF-Restormer (off)	0.89	<b>4.53</b>	0.95	<b>4.61</b>	1.01	<b>4.54</b>	0.97	<b>4.62</b>									
TF-Restormer (off) <sup>‡</sup>	<b>0.81</b>	4.42	<b>0.82</b>	4.58	<b>0.82</b>	4.40	<b>0.81</b>	4.57									
Noisy-distorted (GSR + SSR)																	
Input	3.36	1.91	3.49	1.91	3.64	1.91	3.48	1.73									
VoiceFixer <sup>†</sup>	1.36	3.73	1.35	3.91	1.40	3.80	-	-									
StoRM	1.76	3.97	-	-	-	-	-	-									
UNIVERSE++	1.79	3.39	-	-	-	-	-	-									
TF-Restormer (off)	<b>1.16</b>	<b>4.49</b>	<b>1.21</b>	<b>4.54</b>	<b>1.18</b>	<b>4.52</b>	<b>1.18</b>	<b>4.54</b>									
TF-Restormer (on)	1.30	4.42	1.31	4.49	1.30	4.46	1.26	4.46									

focusing on denoising. In Table 2, we compare against DB-AIAT (Yu et al., 2022), MP-SENet (Lu et al., 2023), and TF-Locoformer as dedicated denoising models, and VoiceFixer, UNIVERSE, and FINALLY as universal restoration baselines. Since the input speech is already well preserved and only corrupted by additive noise, it favors models that minimize unnecessary generation and faithfully retain the input signal. Accordingly, dedicated denoising models outperform universal restoration models in terms of signal fidelity, as they are optimized to suppress noise without altering intact regions. In contrast, restoration models risk degrading reliability by over-modifying clean inputs, making them less trustworthy for such simple cases. While not surpassing dedicated denoising models in raw signal metrics, TF-Restormer achieves more consistent gains, showing strong generalization despite being designed for universal restoration. We additionally include a dedicated TF-Restormer variant; as expected, this task-matched version achieves the higher signal-fidelity scores.

Table 4. Evaluation of non-intrusive MOS results on real-recorded data from VoxCeleb and URGENT 2025 blind testset.

Model	UTMOS	DNSMOS	Model	UTMOS	NISQA	DNSMOS
Input	2.76	2.72	Input	1.55	1.58	1.90
VoiceFixer	2.60	3.08	Bobbsun(R.1)	2.09	3.22	2.88
DEMUCS	3.51	3.27	rc(R.2)	2.03	2.92	2.83
StoRM	3.29	3.17	Xiaobin(R.3)	2.16	3.24	2.92
HiFi-GAN-2	3.67	3.32	wataru9871(R.13)	2.53	3.74	3.10
FINALLY	<b>4.05</b>	3.31	LLaSE-G1	2.09	2.93	2.80
TF-Restormer	3.98	<b>3.34</b>	UniSE	2.85	3.72	<b>3.17</b>
(a) VoxCeleb			TF-Restormer	<b>3.37</b>	<b>4.37</b>	3.13
			(b) URGENT 2025 blind test set			

Finally, we experiment on the SSR task in Table 3, using a single model that directly supports arbitrary output sampling rates. For clean cases, we compare against dedicated super-resolution models: NVSR (Liu et al., 2022a), Freepainter (Kim et al., 2024), and AP-BWE (Lu et al., 2025), as well as VoiceFixer as a universal restoration baseline. As in Table 2, since the low-band of the input speech remains intact, dedicated models that concentrate on reconstructing the upper bands are favored. Unlike conventional approaches that rely on fixed input–output rates and often require zero-padding or redundant resampling, TF-Restormer leverages extension queries to dynamically expand the spectrum. With this versatility, TF-Restormer shows stable performance comparable to the dedicated models, faithfully retaining clean low-frequency regions while effectively generating high-frequency components. When the training is optimally aligned with the conventional method, the dedicated version of the proposed model shows improved results. In addition, under noisy-distorted conditions, TF-Restormer simultaneously restores corrupted regions and reconstructs missing high bands, demonstrating robust generalization beyond pure super-resolution. Overall, these results suggest the advantage of our model as a universal restoration framework that achieves bandwidth extension without sacrificing signal fidelity or requiring explicit resampling.

### 5.3. MOS evaluation on additional datasets

**VoxCeleb** We evaluate TF-Restormer on 50 real-recorded utterances (Su et al., 2020) from VoxCeleb1 (Nagrani et al., 2017) and compared with conventional method including DEMUCS (Défossez et al., 2019) and HiFi-GAN-2 (Su et al., 2021). As shown in Table 4(a), TF-Restormer achieves perceptual MOS scores (UTMOS, DNSMOS) comparable to recent vocoder- and diffusion-based models. While FINALLY (Babaev et al., 2024) remains one of the strongest perceptual-quality systems, our unified architecture delivers similarly natural outputs despite not being specialized for perceptual enhancement, demonstrating competitive robustness on real speech recordings.

**URGENT 2025** Finally, we report non-intrusive MOS metrics on the URGENT 2025 blind test set (Saijo et al., 2025) compared to participating teams and lastest models

Table 5. Ablation study on encoder-decoder design. VCTK-ND denote noisy-distorted input from VCTK data in Table 3.

Case	Size(M)	MAC(G)	LSD <sup>↓</sup>	NISQA <sup>↑</sup>
VCTK (SSR, 8 → 16kHz)				
encoder-only	11.6	151.3	2.12	4.21
encoder-decoder w/o MHCA	30.8	252.4	1.04	4.48
encoder-decoder w/ MHCA	30.1	240.8	<b>0.89</b>	<b>4.53</b>
encoder-decoder w/ MHCA( <i>small</i> )	10.9	89.2	1.36	4.38
VCTK (SSR, 8 → 44.1kHz)				
encoder-only	11.6	415.1	3.25	3.49
encoder-decoder w/o MHCA	30.8	340.4	1.35	4.26
encoder-decoder w/ MHCA	30.1	308.4	<b>1.01</b>	<b>4.54</b>
encoder-decoder w/ MHCA( <i>small</i> )	10.9	156.8	1.44	4.21
VCTK-ND (SSR+GSR, 8 → 16kHz)				
encoder-only	11.6	151.3	2.23	3.72
encoder-decoder w/o MHCA	30.8	252.4	1.20	4.33
encoder-decoder w/ MHCA	30.1	240.8	<b>1.16</b>	<b>4.54</b>
encoder-decoder w/ MHCA( <i>small</i> )	10.9	89.2	1.48	4.20

including LLaSE-G1 (Kang et al., 2025) and UniSE (Yan et al., 2025). The official ranking incorporates both non-intrusive and intrusive measures, and the latter tend to favor deterministic bandwidth-preserving approaches while penalizing generative or reconstructive models. As a result, the top-ranked systems (Sun et al., 2025; Chao et al., 2025; Rong et al., 2025) are predominantly deterministic enhancers and generally obtain lower perceptual MOS. In contrast, TF-Restormer achieves natural-sounding outputs with strong non-intrusive MOS scores, showing that the model maintains stable perceptual quality on the URGENT blind test set as well.

### 5.4. Ablation study

To validate the effects of the proposed methods, we conduct an ablation study on scaled log-spectral loss, decoder design, and frequency projection module.

**Encoder-decoder design** In Table 5, we first analyze the contribution of the encoder–decoder structure (See Appendix E for detailed illustration.). The *Encoder-only* model removes the decoder entirely and applies nine encoder blocks after padding the extension queries at the input. Although this variant has a small parameter count (11.6M), its MACs are extremely large (151-415G), since the encoder must jointly infer the observed low band and synthesize the missing high-frequency components. The *w/o MHCA* variant restores the encoder–decoder structure but replaces the freq cross-self module with the freq. self module used in the encoder, preventing the decoder from conditioning on encoder features. Our proposed *w/ MHCA* model incorporates cross-self frequency attention, enabling more reliable reconstruction through encoder-conditioned queries.

To further isolate the effect of architectural design from model size, we additionally include a reduced version of the proposed model (*w/ MHCA (S)*), whose parameter count matches that of the encoder-only configuration. Despite having far fewer MACs than encoder-only, this size-matched variant consistently outperforms the encoder-only model

Table 6. Ablation study on SFI-discriminator and frequency projection layer in freq. module

STFT-Disc.	PESQ $\uparrow$	UTMOS $\uparrow$	Case	Size(M)	PESQ $\uparrow$	UTMOS $\uparrow$
			UNIVERSE (GSR)			
UNIVERSE (GSR)			w/o F-proj.	28.1	2.26	3.90
Separate	2.27	4.08	w/F-proj.(sep.)	63.6	<b>2.31</b>	<b>4.11</b>
Shared (SFI)	<b>2.29</b>	<b>4.10</b>	w/F-proj.(sha.)	30.1	2.29	4.10
<b>VCTK+DEMAND (DN)</b>						
Separate	3.28	4.07	w/o F-proj.	28.1	3.21	4.03
			w/F-proj.(sep.)	63.6	3.38	<b>4.15</b>
Shared (SFI)	<b>3.41</b>	<b>4.14</b>	w/F-proj.(sha.)	30.1	<b>3.41</b>	4.14
<b>VCTK (SSR, 8 → 16kHz)</b>						
Separate	3.64	4.10	w/o F-proj.	28.1	3.54	3.97
			w/F-proj.(sep.)	63.6	3.545	3.94
Shared (SFI)	<b>3.70</b>	<b>4.11</b>	w/F-proj.(sha.)	30.1	<b>3.70</b>	<b>4.11</b>

(a) Effect of discriminator

(b) Effects of frequency projection

across all bandwidth settings (Table 5(b)), confirming that the gains arise from the explicit separation of analysis and reconstruction and the use of cross-attention rather than increased parameter count or computational cost.

**SFI-STFT discriminator** As shown in Table 6(a), a *shared SFI-STFT* discriminator consistently outperforms *separate rate-specific* discriminators across all tasks. Because the SFI representation aligns TF structure across sampling rates, the unified discriminator receives more coherent supervision and produces more stable gradients. In contrast, separate discriminators see only partial bandwidth conditions, leading to weaker adversarial signals. These results confirm that the shared SFI design is more effective for multi-rate restoration.

**Effects of frequency projection** Finally, we examine the influence of the *frequency-projection (F-proj.)* module. Introducing projection provides an explicit structural prior along the frequency axis, which stabilizes training and yields consistent improvements over the no-projection baseline across tasks. The difference between using *shared* and *separate* projections is relatively small, though the *separate* version exhibits less stable behavior in the super-resolution setting. More critically, the non-shared design is highly inefficient, expanding the model to 63.6M parameters. Given the similar performance and the large gap in model size, the shared frequency-projection module offers the most practical and efficient configuration.

**Effects of scaled log-spectral loss** In Table 7, we assess whether auxiliary spectral losses provide benefits. Using perceptual loss alone leads to less stable optimization, whereas adding any spectral term consistently improves performance, confirming the importance of spectral constraints. Among regression-based losses, the  $\ell_1$  loss on complex STFT components (magnitude, real, imaginary) outperforms magnitude-only variants by better preserving signal fidelity. Replacing  $\ell_1$  with  $\ell_2$  slightly degrades performance, likely due to oversmoothing. These results indicate

Table 7. Ablation study on spectral loss.  $\log 1p$  denotes  $\log(1 + d)$  while  $s\log 1p$  is the proposed scaled  $\log 1p w \log(1 + d/w)$  where  $d$  is  $\ell_1$  distance.

Type of spectral loss	$\mathcal{L}_p$	UNIVERSE(GSR)			VCTK(SSR,8→16kHz)		
		PESQ $\uparrow$	MCD $\downarrow$	UTMOS $\uparrow$	PESQ $\uparrow$	MCD $\downarrow$	UTMOS $\uparrow$
None	✓	1.85	7.23	4.02	3.05	2.47	4.11
$\ell_1$ -norm (mag.)	✓	2.07	6.03	<b>3.82</b>	3.42	2.10	<b>4.10</b>
$\ell_1$ -norm	✓	<b>2.23</b>	<b>5.70</b>	3.76	<b>3.48</b>	<b>1.86</b>	4.07
$\ell_2$ -norm	✓	2.21	5.81	3.70	3.44	1.88	4.06
$\ell_1$ -norm		2.19	5.89	3.71	3.35	2.23	3.91
$\log 1p$ ( $w = 1$ )	✓	2.25	5.72	3.79	3.53	1.83	4.06
$s\log 1p$ ( $w = 10^{-3}$ )	✓	<b>2.27</b>	<b>5.17</b>	<b>3.98</b>	<b>3.67</b>	<b>1.37</b>	4.07
$s\log 1p$ ( $w = 10^{-4}$ )	✓	2.01	5.94	4.07	3.40	2.43	<b>4.10</b>
$s\log 1p$ ( $w = 10^{-3}$ )		2.18	6.05	3.74	3.27	1.88	3.94
$s\log 1p$ (adap. $w_{tf}$ )	✓	<b>2.29</b>	<b>4.96</b>	<b>4.10</b>	<b>3.70</b>	<b>1.29</b>	<b>4.10</b>

that perceptual loss is essential for high-level quality but must be paired with an appropriate spectral objective.

We next compare log- and scaled log-spectral formulations. A plain  $\log 1p$  loss behaves similarly to  $\ell_1$  because typical spectral distances are far below 1, keeping its gradient near 1. The proposed scaled log-spectral loss provides additional gains by adjusting gradient magnitude according to the target spectrum: suitable scale values balance well-aligned and poorly aligned regions, whereas overly small scales collapse gradients and damage performance. Removing perceptual loss noticeably harms both  $\ell_1$  and  $s\log 1p$ , and in this setting  $\ell_1$  remains more stable, showing that  $s\log 1p$  is not effective as a standalone objective. The best overall results arise when  $w_{tf}$  is adaptively derived from the target magnitude, demonstrating that the proposed magnitude-adaptive scaling offers the most reliable trade-off between fine spectral detail and global coherence.

## 6. Conclusion

We presented TF-Restormer, a framework for speech restoration that explicitly addresses decoupled input–output sampling rates. By adopting a query-based asymmetric modeling strategy, the framework concentrates analysis on the observed input bandwidth while reconstructing missing high-frequency components through a lightweight decoder with frequency extension queries. This design removes reliance on conventional resampling and enables a single model to operate across arbitrary input–output rate pairs.

Extensive evaluations across diverse scenarios, including denoising, super-resolution, and compounded distortions, demonstrate balanced improvements in both signal fidelity and perceptual quality. Moreover, the shared SFI-STFT discriminator and the proposed scaled log-spectral loss ensure stable optimization under heterogeneous configurations. Overall, TF-Restormer establishes a unified framework for speech restoration under realistic and mismatched sampling-rate conditions.

## Impact Statement

We use only public speech corpora and collect no new personal data. We do not attempt speaker re-identification, and we do not redistribute raw audio. Aware of potential misuse (e.g., covert monitoring), we will apply access controls and intended-use restrictions and require legal compliance for any release.

## References

Ba, J. L., Kiros, J. R., and Hinton, G. E. Layer Normalization, 2016.

Babaev, N., Tamogashev, K., Saginbaev, A., Shchekotov, I., Bae, H., Sung, H., Lee, W., Cho, H.-Y., and Andreev, P. FINALLY: fast and universal speech enhancement with studio-like quality. In Globerson, A., Mackey, L., Belgrave, D., Fan, A., Paquet, U., Tomczak, J., and Zhang, C. (eds.), *Proc. Adv. Neural Inf. Process. Syst. (NeurIPS)*, volume 37, pp. 934–965. Curran Associates, Inc., 2024. doi: 10.52202/079017-0028.

Braun, S., Gamper, H., Reddy, C. K., and Tashev, I. Towards efficient models for real-time deep noise suppression. In *Proc. IEEE Int. Conf. Acoust., Speech Signal Process. (ICASSP)*, pp. 656–660, 2021.

Cao, R., Abdulatif, S., and Yang, B. CMGAN: Conformer-based Metric GAN for Speech Enhancement. In *Proc. Interspeech*, pp. 936–940, 2022.

Chao, R., Cheng, W.-H., La Quatra, M., Siniscalchi, S. M., Yang, C.-H. H., Fu, S.-W., and Tsao, Y. An Investigation of Incorporating Mamba for Speech Enhancement. *arXiv preprint arXiv:2405.06573*, 2024.

Chao, R., Nasretdinov, R., Wang, Y.-C. F., Jukic, A., Fu, S.-W., and Tsao, Y. Universal Speech Enhancement with Regression and Generative Mamba. In *Proc. Interspeech*, pp. 888–892, 2025.

Chen, J., Wang, Z., Tuo, D., Wu, Z., Kang, S., and Meng, H. Fullsubnet+: Channel attention fullsubnet with complex spectrograms for speech enhancement. In *Proc. IEEE Int. Conf. Acoust., Speech Signal Process. (ICASSP)*, pp. 7857–7861. IEEE, 2022a.

Chen, S., Wang, C., Chen, Z., Wu, Y., Liu, S., Chen, Z., Li, J., Kanda, N., Yoshioka, T., Xiao, X., and others. WavLM: Large-scale self-supervised pre-training for full stack speech processing. *IEEE Journal of Selected Topics in Signal Processing*, 16(6):1505–1518, 2022b.

Choi, H.-S., Kim, J.-H., Huh, J., Kim, A., Ha, J.-W., and Lee, K. Phase-aware speech enhancement with deep complex u-net. In *Proc. Int. Conf. Learn. Represent. (ICLR)*, 2018.

Dang, F., Chen, H., and Zhang, P. DPT-FSNet: Dual-Path Transformer Based Full-Band and Sub-Band Fusion Network for Speech Enhancement. In *Proc. IEEE Int. Conf. Acoust., Speech Signal Process. (ICASSP)*, pp. 6857–6861, 2022.

Défossez, A., Usunier, N., Bottou, L., and Bach, F. Music Source Separation in the Waveform Domain. *arXiv preprint arXiv:1911.13254*, 2019.

Défossez, A., Copet, J., Synnaeve, G., and Adi, Y. High Fidelity Neural Audio Compression. *Transactions on Machine Learning Research*, 2023.

Ephraim, Y. and Malah, D. Speech enhancement using a minimum-mean square error short-time spectral amplitude estimator. *IEEE Transactions on acoustics, speech, and signal processing*, 32(6):1109–1121, 1984.

Fukada, T., Tokuda, K., Kobayashi, T., and Imai, S. An adaptive algorithm for mel-cepstral analysis of speech. In *Proc. IEEE Int. Conf. Acoust., Speech Signal Process. (ICASSP)*, volume 1, pp. 137–140 vol.1, 1992.

Gu, A. and Dao, T. Mamba: Linear-Time Sequence Modeling with Selective State Spaces. In *Proc. Conf. Lang. Model. (COLM)*, 2024.

Gupta, A., Wu, J., Deng, J., and Li, F.-F. Siamese Masked Autoencoders. In *Proc. Adv. Neural Inf. Process. Syst. (NeurIPS)*, pp. 40676–40693, 2023.

Han, K., Wang, Y., Wang, D., Woods, W. S., Merks, I., and Zhang, T. Learning Spectral Mapping for Speech Dereverberation and Denoising. *IEEE/ACM Transactions on Audio, Speech, and Language Processing*, 23(6):982–992, 2015.

Han, S. and Lee, J. NU-Wave 2: A General Neural Audio Upsampling Model for Various Sampling Rates. In *Proc. Interspeech*, pp. 4401–4405, 2022.

Hao, X., Su, X., Horaud, R., and Li, X. FullSubNet: a full-band and sub-band fusion model for real-time single-channel speech enhancement. In *Proc. IEEE Int. Conf. Acoust., Speech Signal Process. (ICASSP)*, pp. 6633–6637. IEEE, 2021.

He, K., Chen, X., Xie, S., Li, Y., Dollár, P., and Girshick, R. Masked Autoencoders Are Scalable Vision Learners. In *Proc. IEEE/CVF Conf. Comput. Vis. Pattern Recognit. (CVPR)*, pp. 16000–16009, June 2022.

Ho, J., Jain, A., and Abbeel, P. Denoising diffusion probabilistic models. In Larochelle, H., Ranzato, M., Hadsell, R., Balcan, M., and Lin, H. (eds.), *Proc. Adv. Neural Inf. Process. Syst. (NeurIPS)*, volume 33, pp. 6840–6851. Curran Associates, Inc., 2020.

Hu, Y., Liu, Y., Lv, S., Xing, M., Zhang, S., Fu, Y., Wu, J., Zhang, B., and Xie, L. DCCRN: Deep Complex Convolution Recurrent Network for Phase-Aware Speech Enhancement. In *Proc. Interspeech*, pp. 2472–2476, 2020.

Jeub, M., Schafer, M., and Vary, P. A binaural room impulse response database for the evaluation of dereverberation algorithms. In *Proc. Int. Conf. Digit. Signal Process. (DSP)*, pp. 1–5, 2009.

Ju, Z., Wang, Y., Shen, K., Tan, X., Xin, D., Yang, D., Liu, E., Leng, Y., Song, K., Tang, S., Wu, Z., Qin, T., Li, X., Ye, W., Zhang, S., Bian, J., He, L., Li, J., and Zhao, S. NaturalSpeech 3: Zero-Shot Speech Synthesis with Factorized Codec and Diffusion Models. In *Proc. Int. Conf. Mach. Learn. (ICML)*, 2024.

Kang, B., Zhu, X., Zhang, Z., Ye, Z., Liu, M., Wang, Z., Zhu, Y., Ma, G., Chen, J., Xiao, L., Weng, C., Xue, W., and Xie, L. "LLaSE-g1: Incentivizing generalization capability for LLaMA-based speech enhancement". In Che, W., Nabende, J., Shutova, E., and Pilehvar, M. T. (eds.), *Proc. Annu. Meet. Assoc. Comput. Linguist. (ACL)*, pp. 13292–13305, Vienna, Austria, July 2025. Association for Computational Linguistics.

Kim, S.-B., Lee, S.-H., Choi, H.-Y., and Lee, S.-W. Audio Super-Resolution With Robust Speech Representation Learning of Masked Autoencoder. *IEEE/ACM Transactions on Audio, Speech, and Language Processing*, 32: 1012–1022, 2024.

Koizumi, Y., Zen, H., Karita, S., Ding, Y., Yatabe, K., Morioka, N., Zhang, Y., Han, W., Bapna, A., and Bacchiani, M. Miipher: A Robust Speech Restoration Model Integrating Self-Supervised Speech and Text Representations. In *Proc. IEEE Workshop Appl. Signal Process. Audio Acoust. (WASPAA)*, pp. 1–5, October 2023.

Kong, J., Kim, J., and Bae, J. Hifi-GAN: Generative adversarial networks for efficient and high fidelity speech synthesis. In Larochelle, H., Ranzato, M., Hadsell, R., Balcan, M., and Lin, H. (eds.), *Proc. Adv. Neural Inf. Process. Syst. (NeurIPS)*, volume 33, pp. 17022–17033. Curran Associates, Inc., 2020a.

Kong, Z., Ping, W., Huang, J., Zhao, K., and Catanzaro, B. Diffwave: A versatile diffusion model for audio synthesis. *arXiv preprint arXiv:2009.09761*, 2020b.

Kumar, K., Kumar, R., de Boissiere, T., Gestin, L., Teoh, W. Z., Sotelo, J., de Brébisson, A., Bengio, Y., and Courville, A. C. Melgan: Generative adversarial networks for conditional waveform synthesis. In Wallach, H., Larochelle, H., Beygelzimer, A., d'Alché-Buc, F., Fox, E., and Garnett, R. (eds.), *Proc. Adv. Neural Inf. Process. Syst. (NeurIPS)*, volume 32. Curran Associates, Inc., 2019.

Le Roux, J., Wisdom, S., Erdogan, H., and Hershey, J. R. SDR-half-baked or well done? In *Proc. IEEE Int. Conf. Acoust., Speech Signal Process. (ICASSP)*, pp. 626–630. IEEE, 2019.

Lee, J. and Han, S. NU-Wave: A Diffusion Probabilistic Model for Neural Audio Upsampling. In *Proc. Interspeech*, pp. 1634–1638, 2021.

Lemercier, J.-M., Richter, J., Welker, S., and Gerkmann, T. StoRM: A Diffusion-based Stochastic Regeneration Model for Speech Enhancement and Dereverberation. *IEEE/ACM Transactions on Audio, Speech, and Language Processing*, 31:2724–2737, 2023.

Li, A., Liu, W., Zheng, C., Fan, C., and Li, X. Two heads are better than one: A two-stage complex spectral mapping approach for monaural speech enhancement. *IEEE/ACM Trans. Audio, Speech, Language Process.*, 29:1829–1843, 2021.

Li, A., You, S., Yu, G., Zheng, C., and Li, X. Taylor, Can You Hear Me Now? A Taylor-Unfolding Framework for Monaural Speech Enhancement. In *Proc. IJCAI*, pp. 4193–4200, 2022.

Li, X., Wang, Q., and Liu, X. MaskSR: Masked Language Model for Full-band Speech Restoration. In *Proc. Interspeech*, pp. 2275–2279, 2024.

Liu, H., Choi, W., Liu, X., Kong, Q., Tian, Q., and Wang, D. Neural Vocoder is All You Need for Speech Super-resolution. In *Proc. Interspeech*, pp. 4227–4231, 2022a.

Liu, H., Liu, X., Kong, Q., Tian, Q., Zhao, Y., Wang, D., Huang, C., and Wang, Y. VoiceFixer: A Unified Framework for High-Fidelity Speech Restoration. In *Proc. Interspeech*, pp. 4232–4236, 2022b.

Liu, L., Guan, H., Ma, J., Dai, W., Wang, G., and Ding, S. A Mask Free Neural Network for Monaural Speech Enhancement. In *Proc. Interspeech*, pp. 2468–2472, 2023.

Loshchilov, I. and Hutter, F. Decoupled Weight Decay Regularization. In *Proc. Int. Conf. Learn. Represent. (ICLR)*, 2019.

Lu\*, Y., Li\*, Z., He, D., Sun, Z., Dong, B., Qin, T., Wang, L., and Liu, T.-y. Understanding and Improving Transformer From a Multi-Particle Dynamic System Point of View. In *Proc. Int. Conf. Learn. Represent. (ICLR)*, 2019.

Lu, Y.-X., Ai, Y., and Ling, Z.-H. MP-SENet: A Speech Enhancement Model with Parallel Denoising of Magnitude and Phase Spectra. In *Proc. Interspeech*, pp. 3834–3838. ISCA, August 2023. doi: 10.21437/Interspeech.2023-1441.

Lu, Y.-X., Ai, Y., Du, H.-P., and Ling, Z.-H. Towards High-Quality and Efficient Speech Bandwidth Extension With Parallel Amplitude and Phase Prediction. *IEEE Transactions on Audio, Speech and Language Processing*, 33:236–250, 2025.

Luo, Y. and Mesgarani, N. Conv-TasNet: Surpassing Ideal Time-Frequency Magnitude Masking for Speech Separation. *IEEE/ACM Trans. Audio, Speech, Language Process.*, 27(8):1256–1266, 2019.

Mack, W. and Habets, E. A. P. Declipping Speech Using Deep Filtering. In *Proc. IEEE Workshop Appl. Signal Process. Audio Acoust. (WASPAA)*, pp. 200–204, 2019.

Mao, X., Li, Q., Xie, H., Lau, R. Y. K., Wang, Z., and Smolley, S. P. Least Squares Generative Adversarial Networks. In *Proc. IEEE Int. Conf. Comput. Vis. (ICCV)*, pp. 2813–2821, 2017.

Mittag, G., Naderi, B., Chehadi, A., and Möller, S. Nisqa: A deep cnn-self-attention model for multidimensional speech quality prediction with crowdsourced datasets. In *Proc. Interspeech*, pp. 2127–2131, 2021. doi: 10.21437/Interspeech.2021-299.

Nagrani, A., Chung, J. S., and Zisserman, A. VoxCeleb: a large-scale speaker identification dataset. *arXiv preprint arXiv:1706.08612*, 2017.

Nakamura, S., Hiyane, K., Asano, F., Nishiura, T., and Yamada, T. Acoustical sound database in real environments for sound scene understanding and hands-free speech recognition. In *Proc. Int. Conf. Lang. Resour. Eval. (LREC)*, 2000.

Oord, A. v. d., Dieleman, S., Zen, H., Simonyan, K., Vinyals, O., Graves, A., Kalchbrenner, N., Senior, A., and Kavukcuoglu, K. WaveNet: A generative model for raw audio. *arXiv preprint arXiv:1609.03499*, 2016.

Pascual, S., Bonafonte, A., and Serrà, J. SEGAN: Speech Enhancement Generative Adversarial Network. In *Proc. Interspeech*, pp. 3642–3646, 2017.

Paulus, J. and Torcoli, M. Sampling Frequency Independent Dialogue Separation. In *2022 30th European Signal Processing Conference (EUSIPCO)*, pp. 160–164, 2022.

Quan, C. and Li, X. SpatialNet: Extensively Learning Spatial Information for Multichannel Joint Speech Separation, Denoising and Dereverberation. *IEEE/ACM Transactions on Audio, Speech, and Language Processing*, 32: 1310–1323, 2024.

Reddy, C. K., Gopal, V., and Cutler, R. DNSMOS P. 835: A non-intrusive perceptual objective speech quality metric to evaluate noise suppressors. In *Proc. IEEE Int. Conf. Acoust., Speech Signal Process. (ICASSP)*, pp. 886–890. IEEE, 2022.

Reddy, C. K. A., Gopal, V., Cutler, R., Beyrami, E., Cheng, R., Dubey, H., Matusevych, S., Aichner, R., Aazami, A., Braun, S., Rana, P., Srinivasan, S., and Gehrke, J. The INTERSPEECH 2020 Deep Noise Suppression Challenge: Datasets, Subjective Testing Framework, and Challenge Results. In *Proc. Interspeech*, pp. 2492–2496, 2020.

Richter, J., Welker, S., Lemercier, J.-M., Lay, B., and Gerkmann, T. Speech Enhancement and Dereverberation with Diffusion-based Generative Models. *IEEE/ACM Transactions on Audio, Speech, and Language Processing*, 31: 2351–2364, 2023.

Rix, A. W., Beerends, J. G., Hollier, M. P., and Hekstra, A. P. Perceptual evaluation of speech quality (PESQ)-a new method for speech quality assessment of telephone networks and codecs. In *Proc. IEEE Int. Conf. Acoust., Speech Signal Process. (ICASSP)*, pp. 749–752, 2001.

Rong, X., Wang, D., Hu, Q., Wang, Y., Hu, Y., and Lu, J. TS-URGENet: A Three-stage Universal Robust and Generalizable Speech Enhancement Network. In *Proc. Interspeech*, pp. 863–867, 2025. doi: 10.21437/Interspeech.2025-734.

Saeki, T., Xin, D., Nakata, W., Koriyama, T., Takamichi, S., and Saruwatari, H. UTMOS: UTokyo-SaruLab System for VoiceMOS Challenge 2022. In *Proc. Interspeech*, pp. 4521–4525. ISCA, September 2022.

Saeki, T., Maiti, S., Takamichi, S., Watanabe, S., and Saruwatari, H. SpeechBERTScore: Reference-Aware Automatic Evaluation of Speech Generation Leveraging NLP Evaluation Metrics. In *Proc. Interspeech*, pp. 4943–4947, 2024.

Saijo, K., Wichern, G., Germain, F. G., Pan, Z., and Roux, J. L. TF-Locoformer: Transformer with Local Modeling by Convolution for Speech Separation and Enhancement. In *Proc. Int. Workshop Acoust. Signal Enhance. (IWAENC)*, pp. 205–209, September 2024.

Saijo, K., Zhang, W., Cornell, S., Scheibler, R., Li, C., Ni, Z., Kumar, A., Sach, M., Fu, Y., Wang, W., Fingscheidt, T., and Watanabe, S. Interspeech 2025 URGENT Speech Enhancement Challenge. In *Proc. Interspeech*, pp. 858–862, 2025.

Scheibler, R., Fujita, Y., Shirahata, Y., and Komatsu, T. Universal Score-based Speech Enhancement with High Content Preservation. In *Proc. Interspeech*, pp. 1165–1169, 2024.

Schröter, H., Escalante-B, A. N., Rosenkranz, T., and Maier, A. Deepfilternet: A low complexity speech enhancement framework for full-band audio based on deep filtering. In *Proc. IEEE Int. Conf. Acoust., Speech Signal Process. (ICASSP)*, pp. 7407–7411, 2022.

Schröter, H., Maier, A., Escalante-B, A., and Rosenkranz, T. Deepfilternet2: Towards real-time speech enhancement on embedded devices for full-band audio. In *Proc. Int. Workshop Acoust. Signal Enhance. (IWAENC)*, pp. 1–5, 2022.

Serrà, J., Pascual, S., Pons, J., Araz, R. O., and Scaini, D. Universal speech enhancement with score-based diffusion. *arXiv preprint arXiv:2206.03065*, 2022.

Shin, U.-H., Ku, B. H., and Park, H.-M. TF-CorrNet: Leveraging Spatial Correlation for Continuous Speech Separation. *IEEE Signal Processing Letters*, 32:1875–1879, 2025.

Su, J., Jin, Z., and Finkelstein, A. HiFi-GAN: High-Fidelity Denoising and Dereverberation Based on Speech Deep Features in Adversarial Networks. In *Proc. Interspeech*, pp. 4506–4510. ISCA, October 2020.

Su, J., Jin, Z., and Finkelstein, A. HiFi-GAN-2: Studio-quality speech enhancement via generative adversarial networks conditioned on acoustic features. In *Proc. IEEE Workshop Appl. Signal Process. Audio Acoust. (WASPAA)*, pp. 166–170. IEEE, 2021.

Su, J., Ahmed, M., Lu, Y., Pan, S., Bo, W., and Liu, Y. RoFormer: Enhanced transformer with Rotary Position Embedding. *Neurocomputing*, 568:127063, 2024.

Sun, Z., Li, A., Lei, T., Chen, R., Yu, M., Zheng, C., Zhou, Y., and Yu, D. Scaling beyond Denoising: Submitted System and Findings in URGENT Challenge 2025. In *Proc. Interspeech*, pp. 873–877, 2025.

Thiemann, J., Ito, N., and Vincent, E. The Diverse Environments Multi-channel Acoustic Noise Database (DEMAND): A database of multichannel environmental noise recordings. *Proceedings of Meetings on Acoustics*, 19(1): 035081, May 2013.

Tolstikhin, I. O., Houlsby, N., Kolesnikov, A., Beyer, L., Zhai, X., Unterthiner, T., Yung, J., Steiner, A., Keysers, D., Uszkoreit, J., Lucic, M., and Dosovitskiy, A. MLP-Mixer: An all-MLP Architecture for Vision. In *Proc. Adv. Neural Inf. Process. Syst. (NeurIPS)*, volume 34, pp. 24261–24272. Curran Associates, Inc., 2021.

Valentini-Botinhao, C. and others. Noisy speech database for training speech enhancement algorithms and tts models. 2017.

Wang, S., Li, B. Z., Khabsa, M., Fang, H., and Ma, H. Linformer: Self-Attention with Linear Complexity, 2020.

Wang, Z., Zhu, X., Zhang, Z., Lv, Y., Jiang, N., Zhao, G., and Xie, L. SELM: Speech Enhancement using Discrete Tokens and Language Models. In *Proc. IEEE Int. Conf. Acoust., Speech Signal Process. (ICASSP)*, pp. 11561–11565. IEEE, 2024.

Wang, Z.-Q. and Wang, D. Deep Learning Based Target Cancellation for Speech Dereverberation. *IEEE/ACM Transactions on Audio, Speech, and Language Processing*, 28:941–950, 2020.

Wang, Z.-Q., Cornell, S., Choi, S., Lee, Y., Kim, B.-Y., and Watanabe, S. TF-GridNet: Making time-frequency domain models great again for monaural speaker separation. In *Proc. IEEE Int. Conf. Acoust., Speech Signal Process. (ICASSP)*, pp. 1–5. IEEE, 2023.

Welker, S., Richter, J., and Gerkmann, T. Speech Enhancement with Score-Based Generative Models in the Complex STFT Domain. In *Proc. Interspeech*, pp. 2928–2932, 2022.

Yamagishi, J., Veaux, C., MacDonald, K., and others. Cstr vctk corpus: English multi-speaker corpus for cstr voice cloning toolkit (version 0.92). 2019.

Yan, H., Liu, C., Xue, S., Liang, X., and Xue, Z. UniSE: A unified framework for decoder-only autoregressive lm-based speech enhancement, 2025.

Yao, J., Liu, H., Chen, C., Hu, Y., Chng, E., and Xie, L. GenSE: Generative speech enhancement via language models using hierarchical modeling. In *Proc. Int. Conf. Learn. Represent. (ICLR)*, 2025.

Yu, G., Li, A., Zheng, C., Guo, Y., Wang, Y., and Wang, H. Dual-Branch Attention-In-Attention Transformer for Single-Channel Speech Enhancement. In *Proc. IEEE Int. Conf. Acoust., Speech Signal Process. (ICASSP)*, pp. 7847–7851, May 2022.

Zhang, J., Yang, J., Fang, Z., Wang, Y., Zhang, Z., Wang, Z., Fan, F., and Wu, Z. AnyEnhance: A unified generative model with prompt-guidance and self-critic for voice enhancement. *IEEE Transactions on Audio, Speech and Language Processing*, 33:3085–3098, 2025.

Zhang, W., Saijo, K., Wang, Z.-Q., Watanabe, S., and Qian, Y. Toward Universal Speech Enhancement For Diverse Input Conditions. In *Proc. IEEE Autom. Speech Recognit. Underst. Workshop (ASRU)*, pp. 1–6, February 2023.

Zhao, S., Nguyen, T. H., and Ma, B. Monaural Speech Enhancement with Complex Convolutional Block Attention Module and Joint Time Frequency Losses. In *Proc. IEEE*

*Int. Conf. Acoust., Speech Signal Process. (ICASSP)*, pp.  
6648–6652, 2021.

## A. Details of Training Procedure

### A.1. Simulation of training dataset

**Clean speech source** The model is trained with VCTK training set. VCTK corpus (Yamagishi et al., 2019) is a multi-speaker English corpus containing 110 speakers with different accents. We split it into a training part VCTK-Train and a testing part VCTK-Test. The version of VCTK we used is 0.92. To follow the data preparation strategy of previous restoration studies Liu et al. (2022b), only the *mic1* microphone data is used for experiments, and *p280* and *p315* are omitted for the technical issues. For the remaining 108 speakers, the last 8 speakers, *p360, p361, p362, p363, p364, p374, p376, s5* are split as test set VCTK-Test for super-resolution subtask. Within the other 100 speakers, *p232* and *p257* are also excluded because they are used in the test set VCTK-ND and VCTK+DEMAND datasets. Therefore, the remaining 98 speakers are used as training data.

**Simulation pipeline** To simulate input signal for training, we randomly applied the various distortions based on the pipeline as shown in Figure 3. In particular, we sequentially applied physical and digital distortions. The physical distortions include convolution of transfer function mainly caused by reverberation at indoor environment. We used RIR samples from DNS dataset (Reddy et al., 2022). Note that we compensated time-delay effect from the convolution by applying direct component of RIR to the corresponding target speech signal. Then, as a second physical distortion, we added various background and interfering noises using noise samples (Reddy et al., 2022) and simulated colored gaussian noise. Each noise source is independently applied with signal-to-noise (SNR) ratio ranging from 0 to 20 dB. Then, as a final stage of physical distortion, we applied band pass filtering (BPF) to account for the recording condition of microphone such as occlusion, hardware properties, in this study, we mainly considered occlusion effect for the simulation. Also, to remove the phase distortion from the BPF, we applied as zero-phase filtering because the model does not need to consider these effect, only to make the learning process complicated. As a final step for physical simulation, we randomly scaled the level of signals from -35 to -15 dB Full Scale (dBFS). We also scaled the speech sources along with the corresponding input.

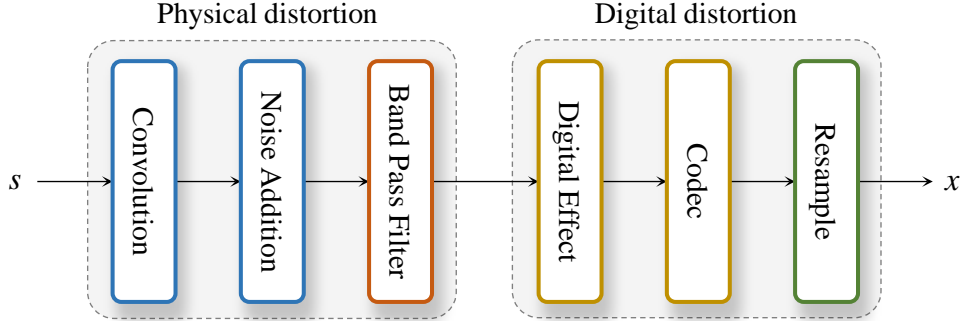


Figure 3. Noisy-distorted speech input simulation pipeline. The simulation procedure is partitioned to physical distortion and digital distortion.

Then, three kinds of digital distortions were simulated in sequence. We randomly applied audio clipping, crystalizer, flanger, and crusher as digital effects, each introducing characteristic nonlinear saturation, spectral over-enhancement, comb filtering, or quantization noise (detailed parameter ranges are summarized in Table 8). Afterward, digital codec compression was applied to emulate transmission artifacts, using either MP3 or OGG (Vorbis/Opus) encoding. Finally, the processed signals were randomly downsampled to 8 or 16 kHz to simulate low-bandwidth recording and communication scenarios.

### A.2. Training Details for Unified Model

For pretraining, TF-Restormer was optimized with a batch size of 2 on a single NVIDIA RTX 6000 Ada 48GB GPU using AdamW (Loshchilov & Hutter, 2019). Pretraining was run for 200,000 steps on the VCTK dataset with 3-second utterances. Adversarial training was then applied for an additional 200,000 steps. We used a learning rate of 2.0e-4 with betas (0.9, 0.995), applying a decay of 0.9 every 10,000 steps after 100,000 steps during pretraining, and every 10,000 steps during adversarial training.

Both stages used a 5,000-step linear warm-up for the generator. In adversarial training, the discriminator was updated twice per generator step (without warm-up), using AdamW with betas (0.8, 0.999). Following multi-scale STFT discriminator

Table 8. List of applied distortions with probabilities and parameter ranges.

Augmentation	Prob.	Param. name	Range / Values	Notes
RIR convolution	0.50	-	-	direct-path delay compensated
Sample Noise	1.00	SNR (dB)	[0, 20]	from DNS dataset
Colored Gaussian Noise	1.00	SNR (dB)	[0, 20]	
		exponent $\beta$	[0.75, 1.5]	
Band-limiting (BPF) (occlusion FIR)	0.5	$f_1$ (Hz)	[500, 1500]	zero-phase
		$f_2$ (Hz)	$f_1 + [200, 500]$	transition band upper edge
		cut_gain	(0.1, 0.3)	stopband gain, applied as $g^\beta$
		$\beta$	[0.25, 1.00]	(thus effective stopband $\approx [0.22, 0.55]$ )
		taps	odd in [31, 61]	firwin2, $f_s=16k$ ( $f_N=8k$ )
Clipping	0.5	level (dB)	[-15, 0]	hard clipping threshold
Crystalizer	0.15	intensity	[1, 4]	spectral “sharpening”
Flanger	0.05	depth	[1, 5]	short-delay comb filtering
Crusher (bit-depth)	0.10	bits	[1, 9]	quantization/aliasing
Codec (any)	0.30	—	—	one of the following
MP3		bit rate (kbps)	[4, 16]	variable bit-rate sampled uniformly
OGG		encoder	vorbis, opus	random choice
Frequency Masking	1.00	$F_{bw}$ (freq. bins)	[0, 10]	
		# masks	[0, 3]	set to [0, 1] in adversarial training
Time Masking	1.00	$T_{dur}$ (frames)	[0, 10]	
		# masks	[0, 2]	set to [0, 1] in adversarial training
Downsample	1.00	target $f_s$	{8k (0.25), 16k (0.75)}	

designs (Défossez et al., 2023), we employed our multi-scale SFI-STFT discriminator with STFT window sizes of [20, 40, 60, 80, 100] ms to capture spectral details at multiple resolutions.

Across all ablation variants, validation loss plateaued around 60k–70k steps, and no architecture exhibited signs of overfitting. We observed that checkpoint selection within this plateau region led to negligible performance differences, indicating that the chosen training length is sufficient for convergence and provides a fair comparison across variants.

### A.3. Training Details for dedicated model

**VCTK+DEMAND** Since noise reduction does not require generating new speech components, prior work has shown that standard supervised learning is often sufficient. Therefore, in the fine-tuning stage we use small weights in adversarial loss ( $\lambda_g = 0.001$  and  $\lambda_{fm} = 0.01$  and the human-feedback perceptual loss ( $\lambda_{hf} = 10^{-5}$ )). The model is trained to perform pure denoising following the standard VCTK+DEMAND training partition. The input and output sampling rates are both fixed to 16 kHz, and thus no extension queries are used in this setting.

**VCTK for Super-resolution** For super-resolution, the model is trained under the same protocol as conventional SR systems, using clean low-band inputs as supervision. Consequently, during adversarial fine-tuning the human-feedback loss is again applied with a small weight ( $\lambda_{hf} = 10^{-5}$ ), as the task primarily focuses on recovering missing high-frequency content.

## B. Details of Model Configuration

For TF-Restormer,  $C_E$  and  $B_E$  for encoder are set to 128 and 6 while  $C_D$  and  $B_D$  are set to 64 and 3. The kernel size in ConvFFN and the number of heads in MHSA/MHCA are commonly set to  $K = 7$  and  $H = 4$ , respectively. For frequency projection layer,  $F_{proj}$  is set to 512.

For offline TF-Restormer, each input mixture is normalized by dividing it by its standard deviation and the enhanced output is rescaled by the same factor. For streaming version of TF-Restormer, two mamba blocks are used in the time module with  $d_{state} = 16$ , causal Conv1D kernel size 3 with expansion factor 4. For streaming version, we still use the non-causal Conv2D layer for input and output projection for robust restoration, therefore the latency increases by two frames, total latency of 80ms (40 ms window, 20 ms hop). Overall, the model size of TF-Restormer is 30.1M for offline mode and 19.0M for streaming mode, which are smaller sizes compared to the existing models.

Table 9. Comparison of the model size and RTF. RTF is calculated on NVIDIA RTX 4090. <sup>†</sup>We utilized pretrained models from open implementation code from UNIVERSE++ (Scheibler et al., 2024). <sup>‡</sup>The model size of FINALLY includes WavLM whose model size is 358M.

Model	Model Size (M)	$f_E \rightarrow f_D$ (kHz)	MACs(G)	RTF
VoiceFixer	70.3	44.1 $\rightarrow$ 44.1	12.9	0.010
StoRM	55.1	16 $\rightarrow$ 16	156.4	0.520
UNIVERSE <sup>†</sup>	46.4	16 $\rightarrow$ 16	36.9	0.014
UNIVERSE++ <sup>†</sup>	84.2	16 $\rightarrow$ 16	36.9	0.015
FINALLY <sup>‡</sup>	454.0	16 $\rightarrow$ 48	—	—
		16 $\rightarrow$ 16	246.9	0.025
TF-Locoformer	14.9	48 $\rightarrow$ 48	731.6	0.088
		8 $\rightarrow$ 16	240.8	0.009
		8 $\rightarrow$ 44.1	308.4	0.017
TF-Restormer	30.1	16 $\rightarrow$ 16	440.9	0.034
		16 $\rightarrow$ 48	518.7	0.053
		8 $\rightarrow$ 16	114.7	0.012
TF-Restormer- <i>streaming</i>	19.0	8 $\rightarrow$ 44.1	138.1	0.018
		16 $\rightarrow$ 16	214.5	0.035
		16 $\rightarrow$ 48	242.0	0.049

### B.1. Comparison of the model size and RTF

In Table 9, we compare model size and multiply-accumulate operations (MACs) for a 1-second-long input using *ptflops* package<sup>1</sup>. We also measure real-time factor (RTF) measured on 4-second-long samples with an NVIDIA RTX 4090. Conventional models operate at fixed input–output sampling rates, which results in fixed MACs regardless of the task configuration. In contrast, TF-Restormer adapts its computation depending on the input and output rates  $f_E$  and  $f_D$ .

Among baselines, StoRM requires 50 diffusion steps, leading to very high MACs and RTF despite its moderate model size. UNIVERSE and UNIVERSE++ reduce the number of steps (8 by default in the open implementation), which lowers the runtime cost compared to StoRM, but their model sizes remain relatively large and the diffusion process cannot be adapted for streaming, representing a fundamental limitation. TF-Locoformer, built on a dual-path design, involves higher computational complexity but benefits from effective parallelism, so its RTF is not as large as its MACs might suggest; its parameter size is also smaller than most diffusion- or vocoder-based systems.

Our proposed TF-Restormer also follows a dual-path formulation, so the raw MACs are relatively large. Nevertheless, RTF remains low in practice, comparable to or even faster than prior dual-path models. Crucially, TF-Restormer optimizes computation according to the input and output sampling rates: for instance, in the 8  $\rightarrow$  16 kHz setting, redundant high-frequency processing is skipped, yielding a very low RTF. Also, the streaming variant maintains consistently low RTF while preserving accuracy, demonstrating its suitability for real-time applications.

### C. Simulation of VCTK Noisy Distorted Input

The noisy-distorted input from VCTK testset in Table 3 was generated by corrupting clean VCTK utterances with additive noise from DEMAND (Thiemann et al., 2013) and colored Gaussian noise, RIR samples from RWCP (Nakamura et al., 2000) and AIR (Jeub et al., 2009) for reverberation, and distortions such as clipping and band-limiting. Additional digital effects including audio codecs (MP3, OGG) were applied before resampling to various rates (8-48 kHz). This simulation aligns the training pipeline while maintaining samples partitioning of speech, noise, and RIR sources. As a result, the average SDR of input data (in case of  $f_E = 16$  kHz) is 2.11dB from 2937 utterances. 998 utterances (about 34%) are below SDR=0 dB and 234 utterances (about 8%) are below SDR=-5 dB.

The details of parameter range are summarized in Table 10.

Table 10. List of applied distortions with probabilities and parameter ranges.

Augmentation	Prob.	Param. name	Range / Values	Notes
RIR convolution	0.50	-	-	direct-path delay compensated
Sample Noise	1.00	SNR (dB)	[5, 20]	from DNS dataset
Colored Gaussian Noise	1.00	SNR (dB)	[5, 20]	
		exponent $\beta$	[0.75, 1.5]	
Band-limiting (BPF) (occlusion FIR)	0.20	$f_1$ (Hz)	[2000, 4000]	zero-phase
		$f_2$ (Hz)	$f_1 + [200, 500]$	transition band upper edge
		cut_gain	(0.1, 0.3)	stopband gain, applied as $g^\beta$
		$\beta$	[0.25, 0.75]	(thus effective stopband $\approx [0.22, 0.55]$ )
		taps	odd in [31, 61]	firwin2, $f_s=16k$ ( $f_N=8k$ )
Clipping	0.20	level (dB)	[-10, 0]	hard clipping threshold
Crystallizer	0.10	intensity	[1, 2]	spectral “sharpening”
Flanger	0.05	depth	[1, 3]	short-delay comb filtering
Crusher (bit-depth)	0.10	bits	[1, 5]	quantization/aliasing
Codec (any)	0.25	—	—	one of the following
MP3		bit rate (kbps)	[16, 64]	variable bit-rate sampled uniformly
OGG		encoder	vorbis, opus	random choice
Frequency Masking	1.00	$F_{bw}$ (freq. bins)	[0, 5]	
		# masks	[0, 1]	
Time Masking	1.00	$T_{dur}$ (frames)	[0, 5]	
		# masks	[0, 1]	

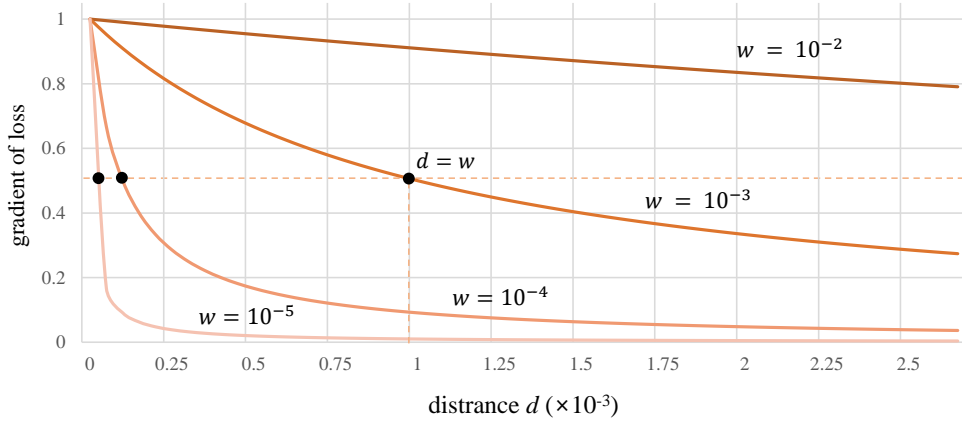


Figure 4. Gradient profiles of the proposed scaled log-spectral loss  $\partial\ell/\partial d = w/(d + w)$  for different scale factors  $w$ . The curves show that the gradient is 1 near zero error and monotonically decreases as the distance  $d = |y - s|$  grows. Smaller  $w$  values make the loss more sensitive to fine spectral deviations, while larger  $w$  values maintain stronger gradients over broader error ranges.

## D. Ablation Details

### D.1. Effects of scaled log-spectral loss

Figure 4 illustrates the gradient behavior of the proposed scaled log-spectral loss, defined as  $\partial\ell/\partial d = w/(d + w)$  where  $d = |y - s|$  denotes the spectral distance and  $w$  is a scale factor. Unlike conventional  $\ell_1$  or  $\ell_2$  criteria, whose gradients are either constant regardless of error magnitude ( $\ell_1$ ) or increase proportionally with larger errors ( $\ell_2$ ), the proposed formulation yields gradients that are strongest near  $d \approx 0$  and gradually diminish once  $d$  exceeds  $w$ . This mechanism emphasizes regions where the spectrum is already well-aligned, thereby preserving fine details, while suppressing unstable updates from heavily corrupted regions. The figure shows that when  $d = w$ , the gradient magnitude stabilizes at 0.5, providing a natural balance between emphasizing accurate components and de-emphasizing severely mismatched ones. As  $w$  decreases, the loss becomes more sensitive to smaller deviations, further suggesting subtle spectral structures that are otherwise neglected in conventional losses.

<sup>1</sup><https://github.com/sovrasov/flops-counter.pytorch>

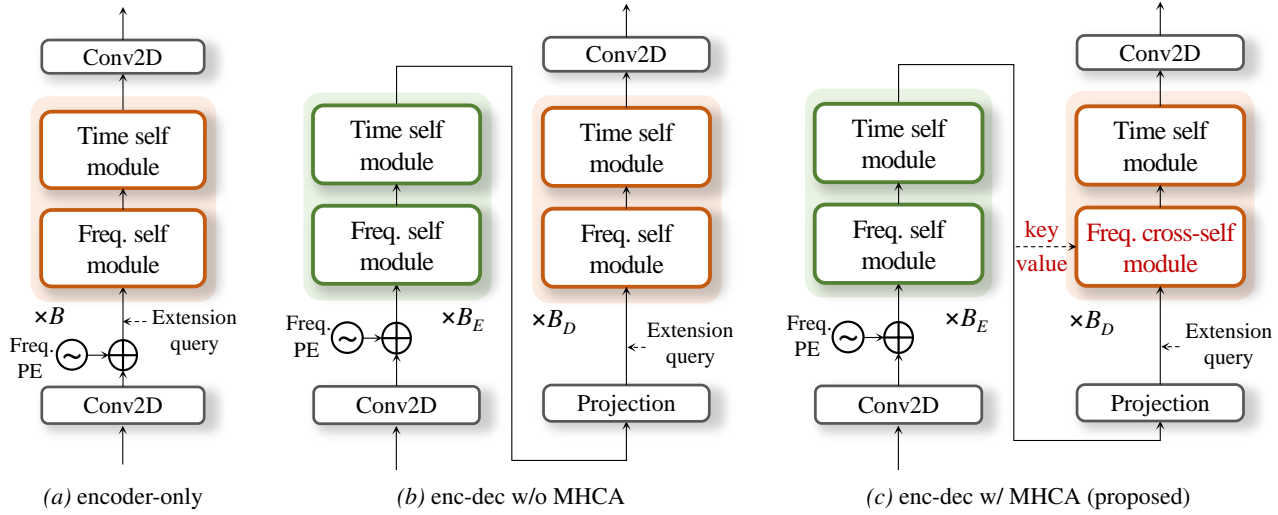


Figure 5. **Unit modules in TF-Encoder and TF-Decoder.** The (a) time module is based on MHSA with RoPE while (b) the frequency encoder module is based on MHSA with frequency projection layer. (c) The frequency decoder module utilize MHCA based on key/value from the encoder features

## D.2. Illustration of encoder-decoder structure ablation

Figure 5 provides detailed comparisons of the three decoder designs considered in our ablation.

**(a) Decoder-only.** This variant directly inserts extension queries into the decoder without an encoder counterpart. The decoder therefore bears the full burden of modeling both the observed input band and the missing high-frequency bands, resulting in heavier computation and weaker inductive bias from the input.

**(b) Encoder-decoder without MHCA.** Here the encoder first analyzes the input bandwidth, and the decoder has the same internal structure as the encoder but receives projected extension queries. Although this design separates analysis and reconstruction, the decoder relies only on self-attention within the extended sequence, and does not explicitly exploit encoder features for reconstruction.

**(c) Encoder-decoder with MHCA (proposed).** In our final design, the decoder additionally uses a frequency cross-self module, where encoder outputs serve as key-value inputs for cross-attention while extension queries act as queries. This enables direct conditioning of high-frequency synthesis on encoder features, while the self-attention within the decoder refines spectral structure among extended bins. As a result, the encoder specializes in processing the observed input, and the lightweight decoder focuses on plausible high-frequency generation guided by encoder information.

These illustrations highlight how the proposed encoder-decoder with MHCA achieves a clear division of labor: the encoder concentrates on input-bandwidth analysis, and the decoder selectively extends spectral content with cross-conditioning, leading to better efficiency and stability compared to the other two designs.

## E. Extension Query Under Imbalanced Sampling-Rate Distributions

Table 11 analyzes whether extension-query tokens become undertrained when certain sampling rates appear too infrequently during training. For the input-rate ablation (top subtable), performance remains nearly identical to the balanced baseline as long as 8 kHz inputs constitute at least 10% of the data. The differences across  $\{0.10, 0.25, 0.50\}$  distributions are minimal in all target-rate settings, and even the best scores often occur at moderately imbalanced ratios. Noticeable degradation appears only in the extreme 1% case, where the model sees almost no examples of low-band inputs; this leads to modest but consistent drops, particularly for the largest gap ( $8 \rightarrow 44.1$  kHz).

A similar pattern is observed for the output-rate ablation (bottom subtable). When high-frequency target rates (44.1 kHz or 48 kHz) have extremely low probability (1–5%), reconstruction quality decreases for those specific targets, as seen in elevated LSD/MCD values. However, once each output rate is represented with a reasonable frequency (around 10% or more), the performance aligns closely with the uniformly balanced case, and the differences across distributions remain small.

Overall, these results show that extension-query undertraining affects performance only under highly skewed sampling-rate distributions. TF-Restormer remains robust as long as each rate appears with moderate frequency, and balanced or mildly imbalanced settings exhibit negligible differences from the baseline.

Table 11. Ablation study on input/output sampling-rate distributions to evaluate the robustness of extension-query training. Grey rows denote the default distribution used for baseline models.

$f_E$ (Hz)		8 → 16kHz			8 → 44.1kHz			16 → 48kHz		
8k	16k	LSD $\downarrow$	MCD $\downarrow$	NISQA $\uparrow$	LSD $\downarrow$	MCD $\downarrow$	NISQA $\uparrow$	LSD $\downarrow$	MCD $\downarrow$	NISQA $\uparrow$
Input		3.36	11.38	1.91	3.64	11.47	1.91	3.48	11.37	1.73
0.01	0.99	1.48	5.83	4.01	1.46	7.12	4.41	<b>1.15</b>	<b>2.82</b>	4.55
0.10	0.90	1.21	2.82	4.48	1.24	3.20	4.46	1.17	2.85	<b>4.56</b>
0.25	0.75	1.16	2.78	4.49	1.18	3.08	<b>4.52</b>	1.18	2.86	4.54
0.50	0.50	<b>1.14</b>	<b>2.74</b>	<b>4.50</b>	<b>1.17</b>	<b>3.05</b>	4.52	1.20	2.89	4.53

(a) ablation of training  $f_E$  distribution.

$f_D$ (Hz)		8 → 16kHz			8 → 24kHz			8 → 44.1kHz			16 → 48kHz		
16k	24k	44.1k	48k	LSD $\downarrow$	MCD $\downarrow$	NISQA $\uparrow$	LSD $\downarrow$	MCD $\downarrow$	NISQA $\uparrow$	LSD $\downarrow$	MCD $\downarrow$	NISQA $\uparrow$	
Input				3.36	11.38	1.91	3.49	11.60	1.91	3.64	11.47	1.91	3.48
0.49	0.49	0.01	0.01	<b>1.15</b>	<b>2.73</b>	<b>4.51</b>	1.17	3.05	<b>4.52</b>	1.36	4.01	4.49	1.51
0.45	0.45	0.05	0.05	<b>1.15</b>	2.74	<b>4.51</b>	<b>1.16</b>	3.05	4.51	1.20	3.16	4.49	1.27
0.40	0.40	0.10	0.10	1.16	2.76	4.50	<b>1.16</b>	<b>3.04</b>	4.51	1.21	3.15	4.49	1.23
0.25	0.25	0.25	0.25	1.16	2.78	4.49	1.18	3.08	<b>4.52</b>	<b>1.18</b>	<b>3.08</b>	<b>4.52</b>	<b>1.18</b>
													<b>4.54</b>

(b) ablation of training  $f_D$  distribution

## F. Evaluation of Dedicated Model on the URGENT Challenge

In the main paper, we reported non-intrusive MOS results on the URGENT blind test set using the unified TF-Restormer model. Since the blind set does not provide clean references, only MOS-based evaluation is possible. For completeness, we additionally train a dedicated URGENT model and report objective fidelity metrics on the non-blind validation set in the challenge.

For the dedicated URGENT configuration, we follow the official training recipe. Because the benchmark resamples all inputs to the target sampling rate regardless of their original rate, we remove high-frequency bins with negligible power prior to processing, which reduces redundant computation under this matched-rate setting. Apart from this preprocessing, the model is trained under the same conditions required by the challenge.

It is important to note that the URGENT benchmark emphasizes deterministic, fidelity-oriented enhancement (Sun et al., 2025; Chao et al., 2025; Rong et al., 2025). Intrusive metrics are heavily weighted, and top-ranked systems typically rely on large, deterministic architectures optimized exclusively for matched-rate denoising. In contrast, models that based on generative approach to improve perceptual quality generally achieve lower intrusive scores despite producing more natural listening quality.

Under such conditions, a dedicated TF-Restormer variant trained with the URGENT recipe shows moderate improvement in signal fidelity compared to the unified model; however, its performance remains below that of highly specialized deterministic and multi-stage systems and perceptual quality become significantly low. This outcome is expected: the strengths of TF-Restormer—arbitrary input–output sampling-rate handling, frequency-extension mechanisms, perceptually oriented losses, and adversarial training—do not align with the evaluation objectives of URGENT. Consequently, while the unified model yields strong non-intrusive MOS on the blind test set, the dedicated URGENT-trained version does not fully reflect the core advantages of our architecture.

## G. Comparison with Conventional Streaming Enhancement Models

We evaluate TF-Restormer-*streaming* against representative real-time denoising models on the VCTK+DEMAND test set, using PESQ, STOI, and the composite metrics CSIG, CBAK, and COVL commonly adopted in prior enhancement works. Unlike conventional streaming models, which are trained specifically for denoising under matched conditions, TF-Restormer-*streaming* inherits the full unified restoration and bandwidth-extension objective and is trained to handle reverberation, distortion, and bandwidth mismatch simultaneously. As a consequence, its model size and computational cost are substantially larger than lightweight denoisers such as NSNet2, DCCRN, or DeepFilterNet.

Table 12. Evaluation results on URGENT 2025 (non-blind test set)

Model(Team)	Model Type	Rank	intrusive signal fidelity				Semantic fidelity				Non-intrusive quality		
			PESQ $\uparrow$	ESTOI $\uparrow$	SDR $\uparrow$	MCD $\downarrow$	LSD $\downarrow$	sBERT $\uparrow$	SpkSim $\uparrow$	CAcc(%) $\uparrow$	UTMOS $\uparrow$	NISQA $\uparrow$	DNSMOS $\uparrow$
Input baseline	-	-	1.37	0.61	2.53	7.92	5.51	0.75	0.63	81.29	1.56	1.69	1.84
	D	9	2.43	0.80	11.29	3.32	2.84	0.86	0.80	84.96	2.11	2.89	2.94
Bobbsun	D	1	<b>2.95</b>	<b>0.86</b>	<b>14.33</b>	3.01	2.83	<b>0.91</b>	<b>0.85</b>	<b>88.92</b>	2.09	3.22	2.88
USEM(rc)	D	2	2.79	0.85	13.11	<b>2.93</b>	<b>2.94</b>	0.90	0.84	88.05	2.30	3.21	3.01
USEM-Flow(rc)	G	-	1.54	0.59	4.49	6.10	3.91	0.76	0.66	69.07	1.79	2.82	2.50
TS-URGENet(Xiaobin)	D+G	3	2.74	0.84	13.06	3.30	3.08	0.89	0.84	87.94	2.16	3.24	2.92
alindborg	D+G	10	1.99	0.76	7.49	4.51	3.73	0.84	0.77	81.70	2.49	3.96	<b>3.28</b>
wataru9871	G	13	1.36	0.56	-13.88	11.25	7.98	0.82	0.51	79.70	2.53	3.74	3.10
TF-Restormer (original)	D+G	-	1.71	0.71	4.19	4.84	4.32	0.84	0.73	80.21	<b>3.57</b>	<b>4.51</b>	3.25
TF-Restormer (dedicated)	D+G	-	2.60	0.83	11.78	3.18	2.91	0.88	0.82	84.28	2.47	3.43	3.06

In terms of signal fidelity, specialized denoising models remain strong, with FRCRN and DeepFilterNet2 achieving the highest PESQ, CBAK, or STOI scores. Nevertheless, TF-Restormer-*streaming* attains competitive perceptual quality, achieving the highest CSIG score among all models and CBAK/COVL values close to the best discriminative systems. This is notable given that TF-Restormer-*streaming* is not optimized for denoising alone, but operates as a general-purpose restoration model that simultaneously handles reverberant, noisy, and bandwidth-limited inputs.

Overall, these results show that TF-Restormer-*streaming* is, to our knowledge, the first unified restoration and super-resolution model capable of streaming operation, while still providing signal fidelity comparable to denoising-oriented baselines. This demonstrates the feasibility of extending multi-rate, multi-distortion restoration models to real-time settings without sacrificing robustness.

Table 13. Comparison of TF-Restormer-*streaming* with existing real-time denoising models on the VCTK+DEMAND test set. We report standard enhancement metrics (PESQ, STOI, CSIG, CBAK, COVL) along with model size and MACs.

Model	Size (M)	MACs (G/s)	PESQ	CSIG	CBAK	COVL	STOI
Noisy	-	-	1.97	3.34	2.44	2.63	0.921
NSNet2 (Braun et al., 2021)	6.2	0.43	2.47	3.23	2.99	2.90	0.903
DCCRN (Hu et al., 2020)	3.7	14.36	<b>2.54</b>	3.74	3.13	2.75	0.938
FullSubNet+ (Chen et al., 2022a)	8.7	30.06	2.88	3.86	3.42	3.57	0.940
FRCRN (Zhao et al., 2021)	10.3	12.3	<b>3.21</b>	4.23	<b>3.64</b>	<b>3.73</b>	-
DeepFilterNet (Schroter et al., 2022)	1.8	0.11	2.81	4.14	3.31	3.46	<b>0.942</b>
DeepFilterNet2 (Schröter et al., 2022)	2.3	0.356	3.08	4.30	3.40	3.70	0.941
TF-Restormer- <i>streaming</i>	19.0	214.5	2.89	<b>4.37</b>	3.41	3.68	0.937

## H. Evaluation on DNS Challenge Dataset

We further evaluate TF-Restormer on the 2020 DNS (Reddy et al., 2020) test sets to examine both signal fidelity and perceptual quality. Table 14 compares objective fidelity metrics against models specifically optimized for denoising with DNS training dataset. Since our unified model is trained to remove reverberation as well as noise, we report fidelity scores only on the “No Reverb” subset, where the clean references are aligned with our training objective. Under this setting, the unified TF-Restormer shows lower fidelity than DNS-targeted systems such as MFNet, USES, and TF-Locoformer. This gap is expected, as the unified model (i) is trained solely on VCTK, (ii) actively removes reverberation and other distortions, and (iii) incorporates perceptual objectives that may deviate from strict waveform fidelity. When trained in a DNS-specific manner without adversarial objectives, however, the dedicated TF-Restormer variant matches or surpasses prior systems, achieving competitive PESQ, STOI, and SI-SDR scores.

Table 15 presents perceptual DNSMOS scores on both “With Reverb” and “No Reverb” subsets. Here, discriminative models tend to preserve the input structure and thus achieve relatively conservative perceptual gains, as seen with Conv-TasNet and FRCRN. Generative approaches such as SELM, GenSE, MaskSR, and UniSE, which prioritize perceptual naturalness, obtain noticeably higher OVRL scores. TF-Restormer shows perceptual quality on par with these generative systems across all subsets, despite not being trained exclusively for perceptual enhancement. In both reverberant and non-reverberant conditions, it achieves strong SIG and BAK scores and matches the best OVRL scores among recent models, demonstrating that the proposed architecture can deliver high perceptual quality while maintaining reasonable signal fidelity.

Table 14. Comparison of TF-Restormer with previous models on 2020 DNS testsets in terms of signal fidelity. “No Reverb” subset is only compared as the proposed TF-Restormer is trained to remove reverberation.

System	PESQ	STOI(%)	SI-SDR(dB)
Noisy	1.58	91.5	9.1
FullSubNet (Hao et al., 2021)	2.78	96.1	17.3
CTSNet (Li et al., 2021)	2.94	96.2	16.7
TaylorSENet (Li et al., 2022)	3.22	97.4	19.2
FRCRN (Zhao et al., 2021)	3.23	97.7	19.8
MFNet (Liu et al., 2023)	3.43	97.9	20.3
USES (Zhang et al., 2023)	3.46	98.1	21.2
TF-Locoformer (Saijo et al., 2024)	3.72	98.8	<b>23.3</b>
TF-Restormer	2.83	96.4	16.1

Table 15. Comparison of TF-Restormer with previous models on 2020 DNS testsets in terms of perceptual quality (DNS scores). “With Reverb” subset contains reverberation while “No Reverb” subset only involves noise. “D” and “G” denote discriminative and generative methods, respectively.

Model	Type	With Reverb			No Reverb		
		SIG	BAK	OVRL	SIG	BAK	OVRL
Noisy	-	1.76	1.50	1.39	3.39	2.62	2.48
Conv-TasNet (Luo & Mesgarani, 2019)	D	2.42	2.71	2.01	3.09	3.34	3.00
FRCRN (Zhao et al., 2021)	D	2.93	2.92	2.28	3.58	4.13	3.34
SELM (Wang et al., 2024)	G	3.16	3.58	2.70	3.51	4.10	3.26
MaskSR (Li et al., 2024)	G	3.53	4.07	3.25	3.59	4.12	3.34
AnyEnhance (Zhang et al., 2025)	G	3.50	4.04	3.20	3.64	<b>4.18</b>	3.42
GenSE (Yao et al., 2025)	G	3.49	3.73	3.19	3.65	<b>4.18</b>	<b>3.43</b>
LLaSE-G1 (Kang et al., 2025)	G	3.59	4.10	3.33	<b>3.66</b>	4.17	3.42
UniSE(Yan et al., 2025)	G	<b>3.67</b>	4.10	<b>3.40</b>	<b>3.67</b>	4.14	<b>3.43</b>
TF-Restormer	D+G	3.60	<b>4.12</b>	3.35	3.65	<b>4.18</b>	<b>3.43</b>

## I. Limitations and Future Works

Although TF-Restormer demonstrates balanced improvements in both signal fidelity and perceptual quality, several limitations remain.

First, when the input speech is extremely degraded, the uncertainty in the observed spectrum can lead to content or speaker artefacts. This reflects a fundamental trade-off in speech restoration: adversarial training promotes perceptually natural reconstructions by hallucinating plausible high-frequency details, whereas purely supervised objectives remain closer to the reference but often oversmooth, reducing naturalness.

Second, the model may exhibit mild rate-distribution sensitivity. As discussed in Appendix E, severely imbalanced exposure to certain sampling rates (e.g., <1%) can lead to undertrained extension-query regions, particularly at the highest frequencies. Although moderate coverage ( $\approx 10\%$ ) is sufficient in practice, this highlights a remaining limitation of our arbitrary-rate formulation.

Third, because the model is trained on heavily distorted scenarios using limited single-language clean corpora, it may inherit language-specific biases, particularly due to the perceptual loss’s dependency on a pretrained speech model (e.g., WavLM). This could affect cross-lingual generalization to underrepresented phonetic patterns.

Finally, while TF-Restormer addresses universal restoration, it does not handle multi-speaker conditions such as speech separation or speaker extraction. The current formulation assumes a single target speaker and does not incorporate mechanisms for resolving overlapping speech.

Future work includes reducing hallucination artefacts under extreme degradations, improving robustness under highly imbalanced sampling-rate distributions, extending the training pipeline to multilingual and more diverse corpora, and integrating the framework with multi-speaker modeling. Given that the TF dual-path architecture was originally proposed for separation, the proposed model has promising potential for extension to overlapped multi-speaker restoration.